U. S. Department of Energy
National Energy Technology Laboratory
Federal Grant #: DE-FE0031771

FINAL REPORT

Techno-Economic Optimization of Advanced Energy Plants with Integrated Thermal, Mechanical, and Electro-Chemical Storage

Principle Investigator (PI) and Submitting Official:
Dr. Debangsu Bhattacharyya
Chemical and Biomedical Engineering
West Virginia University
Phone: (304) 293-9335
Fax: (304) 293-4139
Debangsu.Bhattacharyya@mail.wvu.edu

Submission Date: July 5, 2023

UEI: M7PNRH24BBM8

Report#: DOE-WVURC-0031771

Recipient Organization:
West Virginia University Research Corporation
86 Chestnut Ridge Road
PO Box 6845
Morgantown, WV 26506-6845
Telephone: 304-293-3998
Fax: 304-293-7435

Project/Grant Period: August 1, 2019 – January 31, 2023

Signature of Submitting Official: 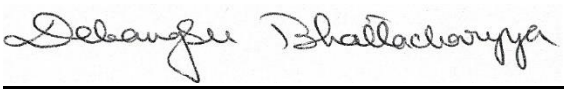

Disclaimer

TABLE OF CONTENTS

LIST OF EXHIBITS

ACRONYMS AND ABBREVIATIONS

ACM	Aspen Custom Modeler
AIC	Akaike Information Criterion
APD	Aspen Plus Dynamics
BBO	Black-box optimization
CAES	Compressed air energy storage
CDI	Control Design Interface
CES	Cryogenic energy storage
CAPEX	Capital expenditure
FFPP	Fossil-fueled power plants
FOM	Full order model
GT	Gas turbine
HRSG	Heat recovery steam generator
HSV	Hankel Singular Value
HTTS	High temperature thermal energy storage
LCOS	Levelized cost of storage
MIMO	Multiple input multiple output
MS	Molten salt
NaS	Sodium sulfur
NGCC	Natural gas combined cycle
OPEX	Operating expenditure
O&M	Operation & Maintenance
PCM	Phase change material
PEM	Polymer electrolyte membrane
PHS	Pumped hydro storage
ROM	Reduced order model
SCPC	Supercritical pulverized coal
ST	Steam turbine
RFB	Redox flow battery
VRFB	Vanadium redox flow battery

1 INTRODUCTION

The increasing use of renewable energy sources is leading to increased cycling of fossil-fueled power plants (FFPP) that are designed to operate at base-loaded conditions. Cycling includes load-following (ramping of the power generated up/down), shutdown and startup, and operation under variable and minimum load conditions. Cycling operation causes increased wear-and-tear of critical equipment items leading to increased capital and operation and maintenance (O&M) costs, decreased plant efficiency, and increased environmental emissions compared to the base-loaded operation. Integrating energy storage facilities with the FFPPs can be helpful in reducing load-following operation of FFPPs. However, the storage technologies differ widely based on the maturity of technologies, their costs, size, life, availability, efficiency, footprint, safety and environmental hazards. Furthermore, the grid scale imbalance can significantly vary based on the location, time of the day and the year.

Energy storage technologies have been mainly evaluated from the perspective of deployment at the grid level or at the solar or wind generation facilities without being tied to any specific FFPP. However, decentralized deployment of energy storage facilities at the FFPP level has considerable advantages due to possibilities of smaller storage capacities, immediate benefits realized by the host power plant due to the increase in the efficiency, cleaner emission and higher plant life to name a few. Most importantly, deployment at the FFPP level can exploit the existing equipment items and facilities at the host power plant, thus reducing the CAPEX and reducing the storage capacity. However, realization of these benefits will critically depend on novel configuration/integration strategies with the least impact on the power plant operation and its configuration. Furthermore, dynamics of the entire integrated system including both the FFPP and the storage technologies must be taken into account to obtain the cost-optimal solution.

With these motivations, the objective of this project was to complete a focused evaluation of decentralized deployments of energy storage facilities at the FFPP level. The project assessed novel configuration/integration strategies that would have the least impact on the power plant operation and its configuration. Furthermore, dynamics of the entire integrated system including both the FFPP and the storage technologies were considered to obtain cost-optimal solutions necessary for appropriate market evaluation. Promising thermal, chemical, mechanical, and electro-chemical storage technologies were evaluated with due consideration of their transient response to obtain various optimal system concepts that can minimize the levelized cost of storage.

The storage technologies that were evaluated by the project team are shown in Exhibit 1-1. For thermal storage, cryogenic energy storage (CES) along with high temperature heat storage in molten salt as well as phase change material (PCM) were evaluated. For mechanical storage, compressed air energy storage (CAES) and pumped hydro storages were evaluated. For chemical storage, hydrogen storage was evaluated. For electrochemical storage, the team evaluated sodium sulfur (NaS) batteries, vanadium redox flow batteries (VRFB) as well as Li-ion batteries (LiBs).

Integration of these storage technologies with the natural gas combined cycle (NGCC) and supercritical pulverized coal (SCPC) plants was considered. However, it should be noted that some of these storage technologies are standalone and some of these technologies are only integrated with the NGCC plant. For example, pumped hydro and VRFB and Li-ion batteries are standalone storage for both NGCC and SCPC plants. However, CAES can be integrated with NGCC since air extraction/injection to GT can be considered and hot air obtained by cooling the NaS batteries can be injected back to the HRSG in NGCC but not to SCPC plant and therefore, CAES and NaS batteries are considered to be standalone while evaluating the SCPC plant.

Exhibit 1-1. Block Flow Diagram of the Evaluated Energy Storage Technologies

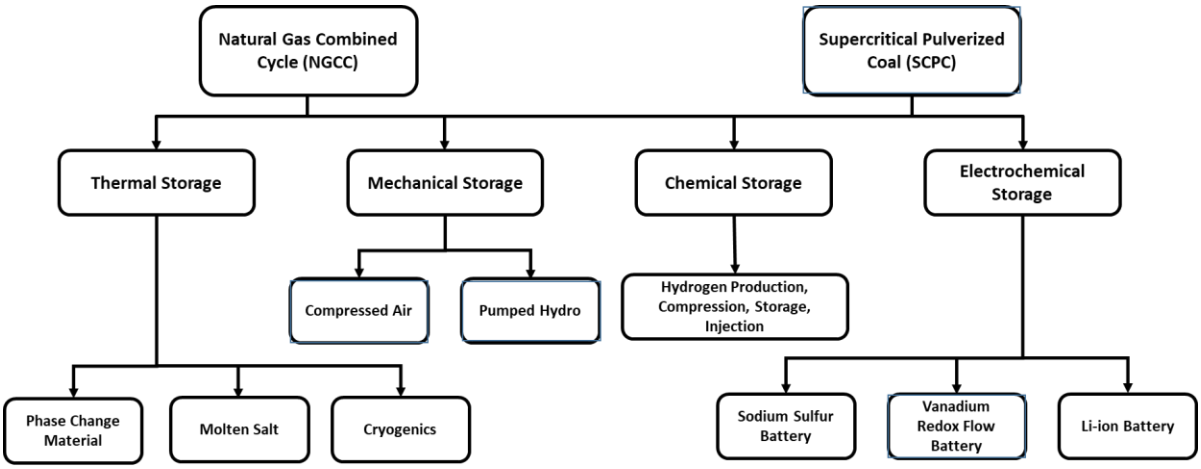

Six technologies, namely molten salt, cryogenics, compressed air, pumped hydro, H_2 storage and Li-ion battery storage, were downselected based on their levelized cost of storage (LCOS). Detailed techno-economic assessment (TEA) of these six technologies was undertaken. Dynamic response of the energy storage technologies along with dynamics of the host power plants were analyzed.

The project included following tasks/subtasks:

- Task 1.0 Project Management and Planning.
- Task 2 – Develop Computational Models for Candidate Storage Technologies
  - Subtask 2.1 – Non-Thermal Energy Storage Technologies
  - Subtask 2.2 – Thermal Energy Storage Technologies
- Task 3 – Storage Model Integration and Simulation
- Task 4 – Reduced Model Development for Storage Technologies
  - 4.1 – Non-Thermal Energy Storage Technologies
  - 4.2 – Thermal Energy Storage Technologies
- Task 5 - Implement Time-Discretization and/or Decomposition-based Algorithms for Energy Storage Technology Selection

- Task 6 - Implement Data-Driven Black-Box Optimization (BBO) Alternative Algorithms for Energy Storage Technology Selection
- Task 7 – Detailed Dynamic Simulation of Promising Storage Technologies
    - 7.1 – Non-Thermal Energy Storage Technologies
    - 7.2 – Thermal Energy Storage Technologies
- Task 8 – Complete TEAs of Promising Storage Technologies

2 CONFIGURATIONS AND MODELS OF NATURAL GAS COMBINED CYCLE PLANT AND ENERGY STORAGE SYSTEMS

NATURAL GAS COMBINED CYCLE (NGCC) PLANT

A diagram of the NGCC plant is shown in Exhibit 2-1.

Exhibit 2-1. Block Flow Diagram of the NGCC Plant with H_2 Injection

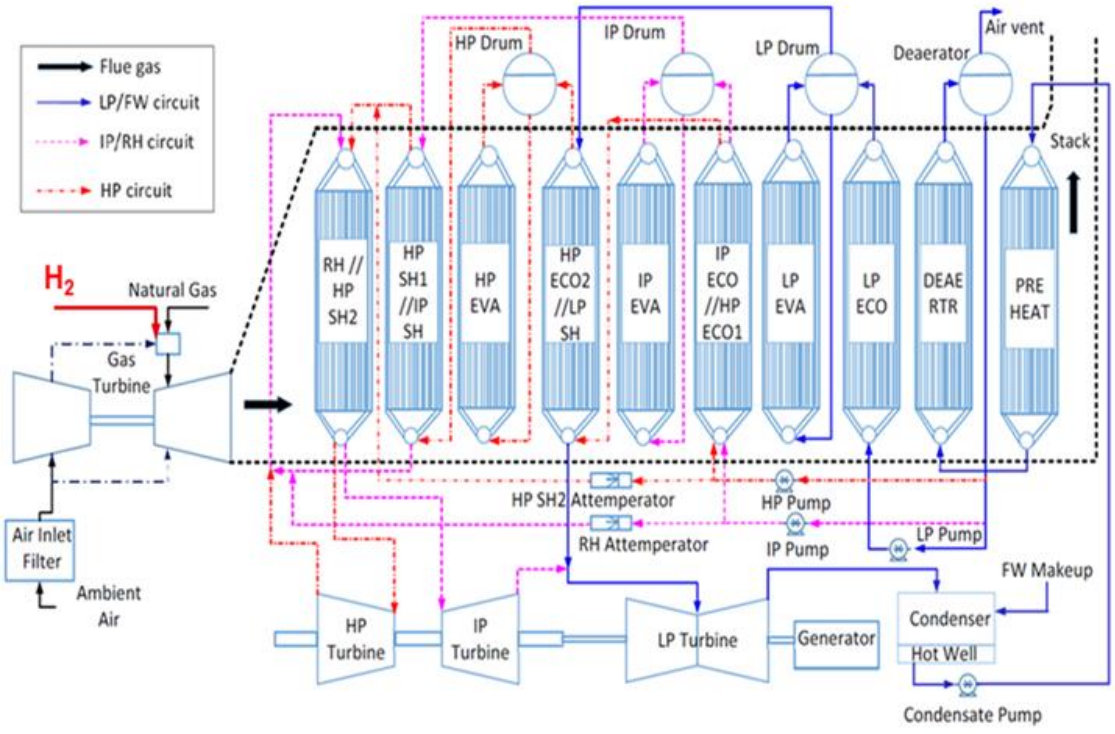

The first-principles model of the NGCC plant used in this work was developed by Wang et al. (2020). The plant-wide model includes models of following components- gas turbine (GT), heat recovery steam generator (HRSG) and steam turbine (ST).

CRYOGENIC ENERGY STORAGE (CES)

Exhibit 2-2 shows the configuration of CES. A simulation based blackbox global optimization approach was developed and used towards the optimization goal. The optimization variables are highlighted in orange while the parameters are highlighted in green. The output variables that are of interest in calculating the efficiency of the system are highlighted in blue. A Bayesian global optimization approach using Gaussian Processes for surrogates towards the goal of global

optimization was used. It is followed by a Limited memory Broyden–Fletcher–Goldfarb–Shanno (L-BFGS) local optimization solver to guarantee local optimality in the region of current global optima.

Convergence within ASPEN flowsheets pose a challenge due to the increased complexity from recycle loops. Thus, the team also developed a convergence algorithm using pseudo-input variables using the fixed-point iteration update algorithm. The expressions for the functional forms in this update were obtained on a subproblem towards convergence using the golden section search algorithm. Having developed this methodology for global optimization of blackbox simulation-based models with internal convergence algorithm, the team modeled the stand-alone CES system and optimized the process configuration for this system. An increased roundtrip efficiency of 52.48% was obtained in this case.

Exhibit 2-2 Cryogenic energy storage flowsheet detailing the storage of liquid air

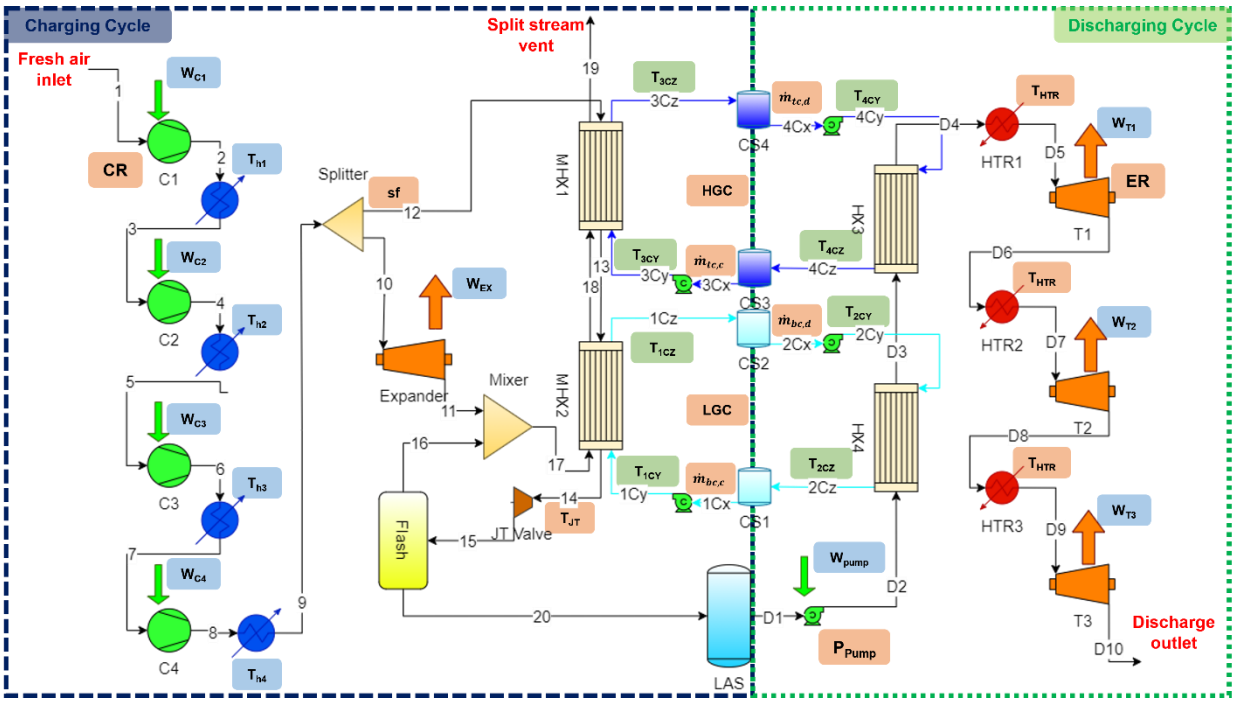

HIGH TEMPERATURE THERMAL ENERGY STORAGE (HTTS)

In the molten salt storage system, the heat transfer fluid (HTF) also serves as the storage medium. Three heat exchangers in series in charging are designed to capture the liquid sensible heat, latent heat, and vapor sensible heat respectfully. As shown in Exhibit 2-3, the typical two-tank system model indicates that such system cannot maintain both high charging efficiency and high hot tank temperature. The molten salt required to capture steam latent heat is much higher than

vapor sensible heat. This motivated us to add a splitter before the last heat exchanger to control the molten salt flow rate. An intermediate hot tank was also introduced to store the excess molten salt, as shown in Exhibit 2-4.

Exhibit 2-3: Molten salt hot tank temperature and charging efficiency versus molten salt flow rate in (a) two-tank model (b) and three-tank model

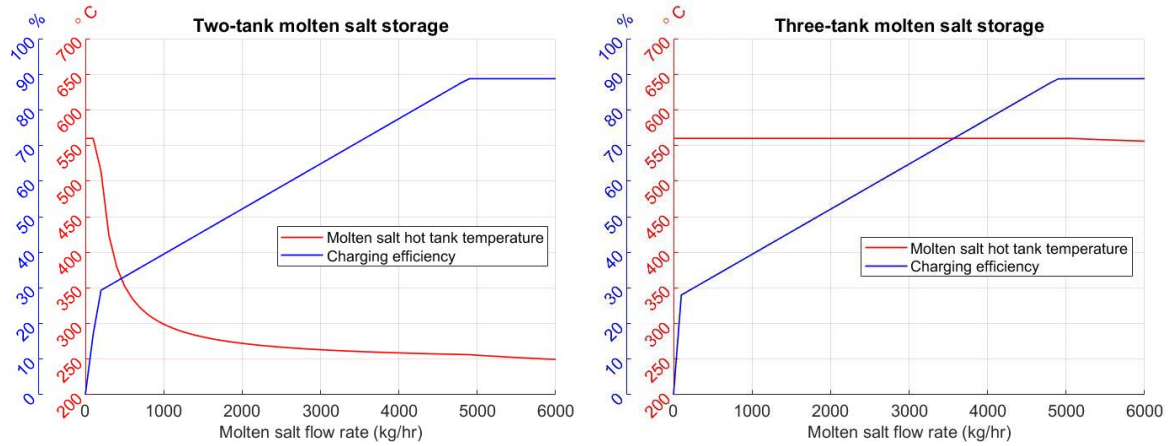

(a) (b)

Exhibit 2-4: Three-tank molten salt storage system

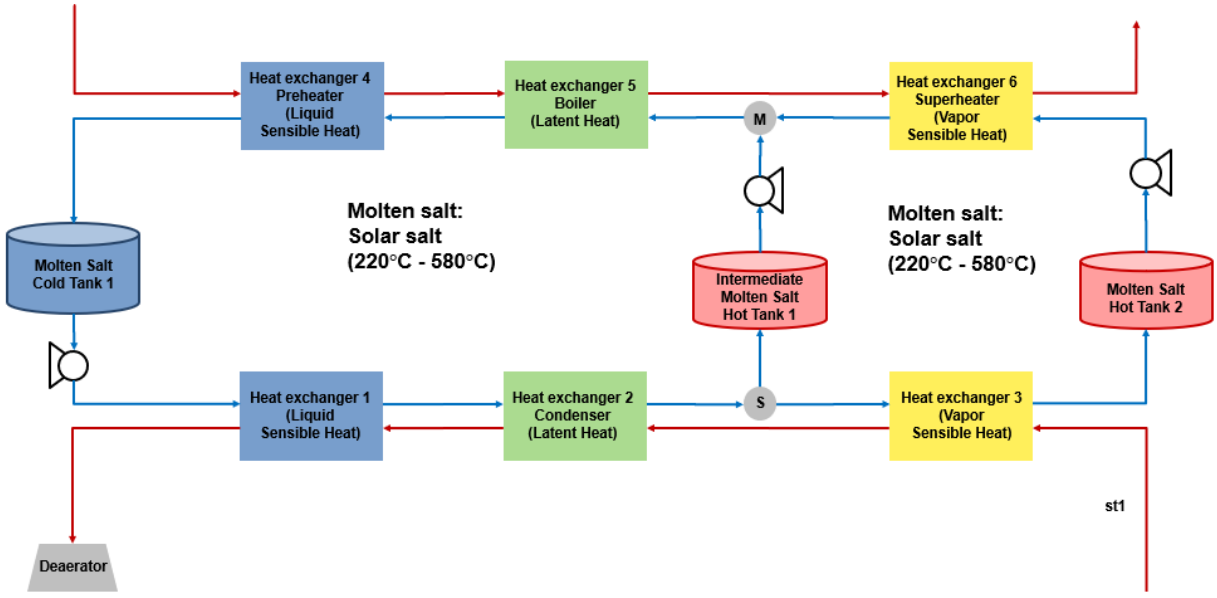

Solar salt was chosen as the storage medium due to its excellent thermal properties as well as the low cost. However, the cold tank temperature is limited by the operating temperature of solar salt. As the steam is designed to exit the system at 150 °C, the solar salt cannot reach below

220 °C. Due to lack of other suitable low-cost option, the team further proposed the four-tank storage system shown in Exhibit 2-5.

Exhibit 2-5: Four-tank molten salt storage system

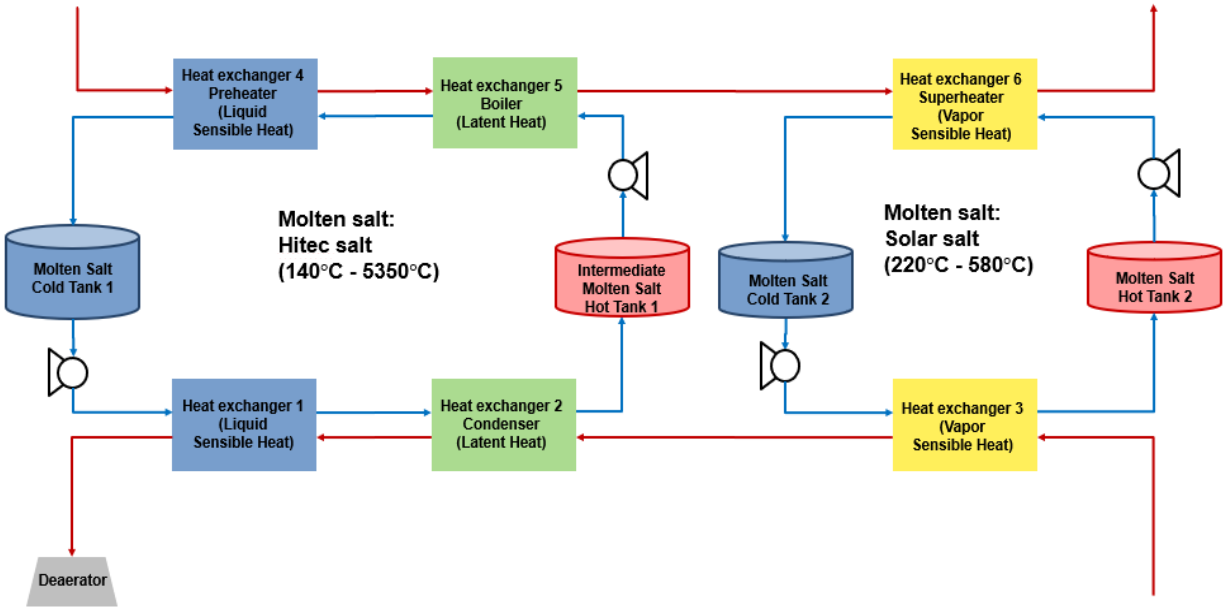

A steady-state model was developed on both Matlab and Aspen, where the extracted steam entering the system was assumed to have constant temperature, pressure and flow rate. The maximum overall efficiency and discharging steam pressure was obtained by setting the inlet and outlet of the molten salt tank the same in the charging and discharging cycle, respectively. From a simple turbine model, power output from the regenerated steam is also calculated.

For flexible integration, such a model can accommodate excess steam at different pressure. Regenerated steam pressure, overall efficiency as well as power output under various load are plotted in Exhibit 2-6 under two models above. Despite discharging steam pressure, the system's general performance is not very susceptible to inlet pressure.

Compared to the three-tank model, the four-tank model has higher efficiency and energy output, but the discharging steam pressure is lower.

Exhibit 2-6: Molten salt storage power output, overall efficiency, and discharging pressure versus inlet pressure for: (a) three-tank system (b) four-tank system

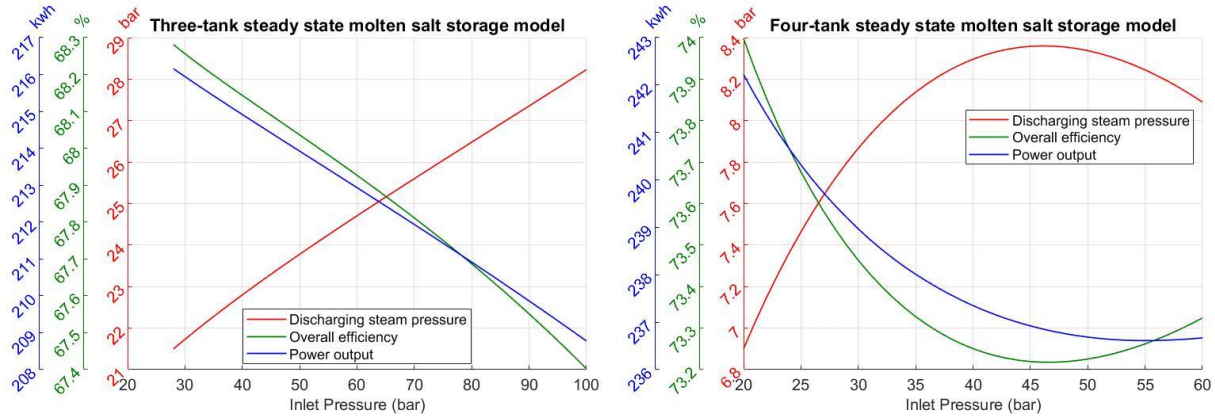

(a) (b)

COMPRESSED AIR ENERGY STORAGE (CAES)

A diagram of the NGCC plant is shown in Exhibit 2-7.

Exhibit 2-7. Block Flow Diagram of the Compressed Air Energy Storage Process

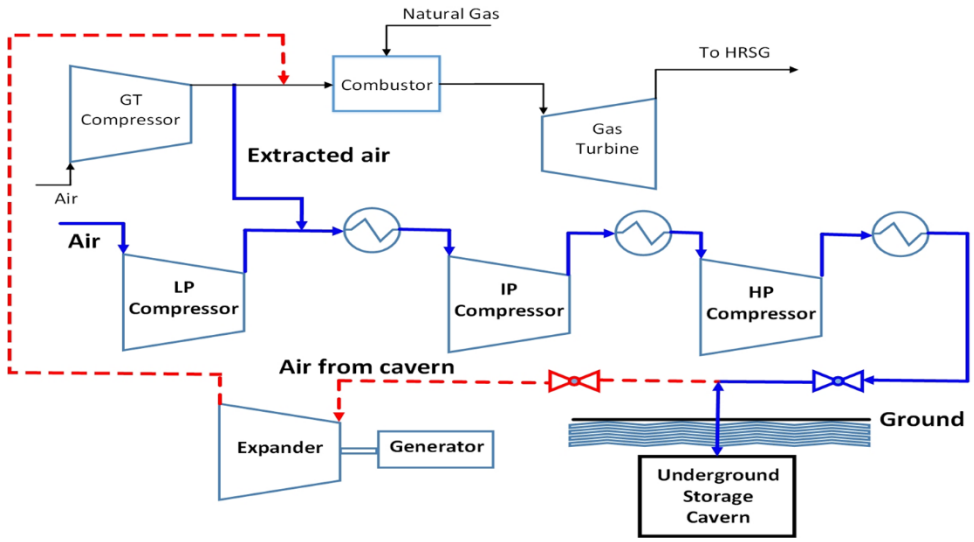

The CAES is integrated with the NGCC plant. For flexibility in integration, the GT compressor and turbine were considered to be detached. When the electricity is in excess, a portion of the air from the GT compressor discharge can be extracted and injected to the intermediate stage of an

auxiliary compressor for air compression. Based on the GT compressor vendor, it may be possible to completely eliminate the low pressure (LP) stage of the compressor extracting the entire quantity of desired extra air for the storage from the GT compressor. This air is further compressed sending it to the cavern. When power is needed, the GT compressor air flowrate can be greatly reduced immediately providing the required power. The shortfall in air to the combustor is provided from the cavern through an expander, which also generates electricity. For added flexibility and for the SCPC plant, the team also considered that the CAES can operate as standalone. Obviously, that option needed dedicated air heating and cooling and additional expanders, but that added to the flexibility especially in consideration if there are constraints on how much air can be extracted from the GT compressor and at what stage and how much air can be injected into the system.

A generic compressor stage model was developed for air that can be used to model any stage irrespective of the compression stage. Since the last stage of the compressor can have high pressure, the model should be applicable to any such stage. Furthermore, during charging to the cavern, the compressor discharge pressure keeps changings. But the GT extraction pressure is not likely to change much thus the compressor inlet pressure is not expected to change appreciably. These variabilities in the compressor ratios will require the design of a suitable control strategy for flow control. While inlet guide vanes are widely used for air compressor flow control, those may not be desired option in this case since it will not be desired to waste the energy by dropping the GT extraction air pressure. A control strategy like variable frequency drive can be considered, but adds to high capital cost. A perfect control is assumed while evaluating the economics. Similarly, during discharging from the cavern, the expander inlet pressure keeps changing, however since the air is discharged to the GT combustor, that expansion ratio will also keep changing with discharging. Thus, it is desired that the model should be able to calculate the power requirement and discharge temperature for a large range of compression ratio over a large range of pressure and temperature as expected for CAES system. In addition, a general heat exchanger model is developed for interstage cooling for the compressor and interstage heating for the expanders. A dynamic model of the cavern is also developed.

Exhibits 2-8 and 2-9 show the dynamics of pressure and temperature variation respectively inside the cavern during discharge phase. The initial temperature and pressure of the compressed air during discharge was 33^{o}C and 69 bar. The mass flowrate during the discharge phase was maintained at a constant flowrate of 417 kg/s till 5 hr (Crotogino et al., 2001). Later, the discharge flowrate was decreased till the simulated period of 15 hr. This effect was shown in the temperature dynamics as the temperature of the storage model decreases to a minimum of 8.8^{o}C during the 10 hr period and then increased slowly due to heat transfer between the cavern wall and fluid. A lumped heat transfer model between the cavern wall and compressed air was considered based on the open literature (Raju and Khaitan, 2012). The model results were compared with the experimental data from the Huntorf plant in Germany and as observed in Exhibits 2-8 and 2-9, the model results compared well with the data.

Exhibit 2-8 Pressure variation inside the cavern during the discharge phase

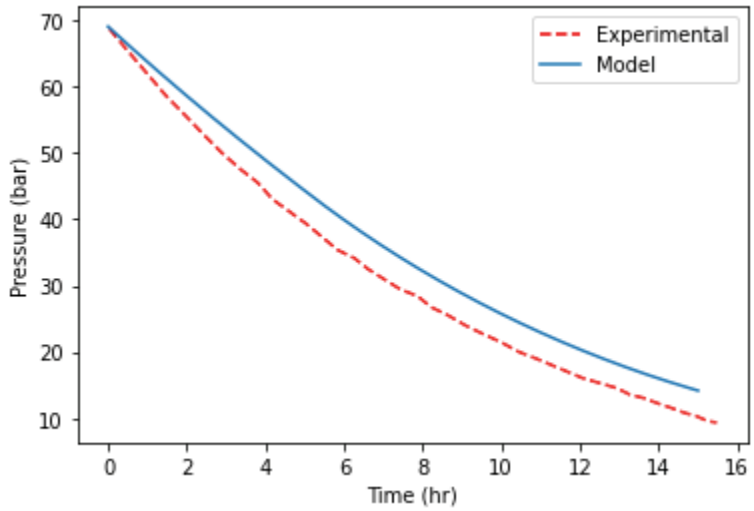

Exhibit 2-9 Temperature variation inside the cavern during the discharge phase

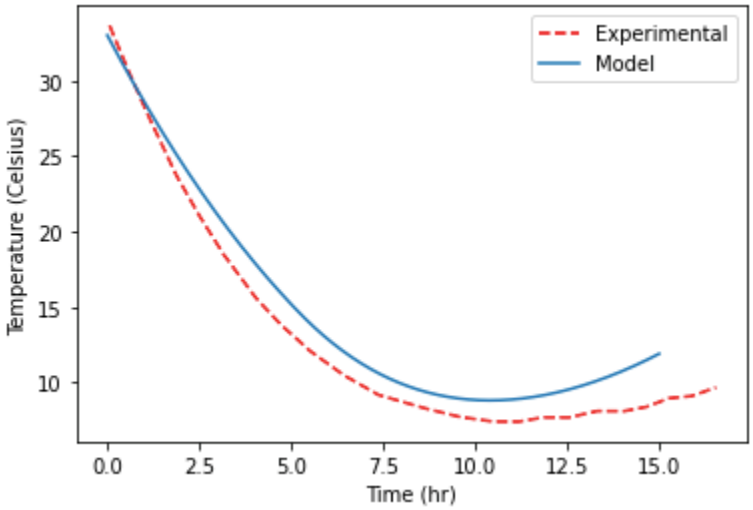

HYDROGEN STORAGE

A dynamic model of the storage system was developed. For hydrogen, real gas thermodynamics was considered (Striednig et al., 2014). The dynamics of temperature and pressure in the hydrogen storage systems play a vital role in optimizing the storage performance.

A dynamic storage model was developed in Aspen Custom Modeler. Based on the data available

in the open literature (Xiao et al., 2016), a small hydrogen cylinder of capacity 150.8 liter was simulated for model validation.

There are three specific cases which were analyzed as follows:

1. Charging and discharging conditions for the case of constant inflow and outflow temperatures.
2. Charging and discharging conditions for the case of variable inflow and outflow temperatures.
3. Charging and discharging conditions for the case of constant inflow and variable outflow temperatures.

Results from the simulation of these cases compared well with the literature.

In addition, a simple model of the polymer electrolyte membrane (PEM) electrolyzer was developed. The PEM technology excels in terms of commercial viability, efficiency and compactness when compared to the other hydrogen production technologies. One of the key advantages of the PEM electrolyzers is the room temperature operation.

A simple schematic diagram of the PEM electrolyzer set up is shown in Exhibit 2-10 (Görgün, 2006).

Exhibit 2-10. Schematic of a PEM electrolyzer

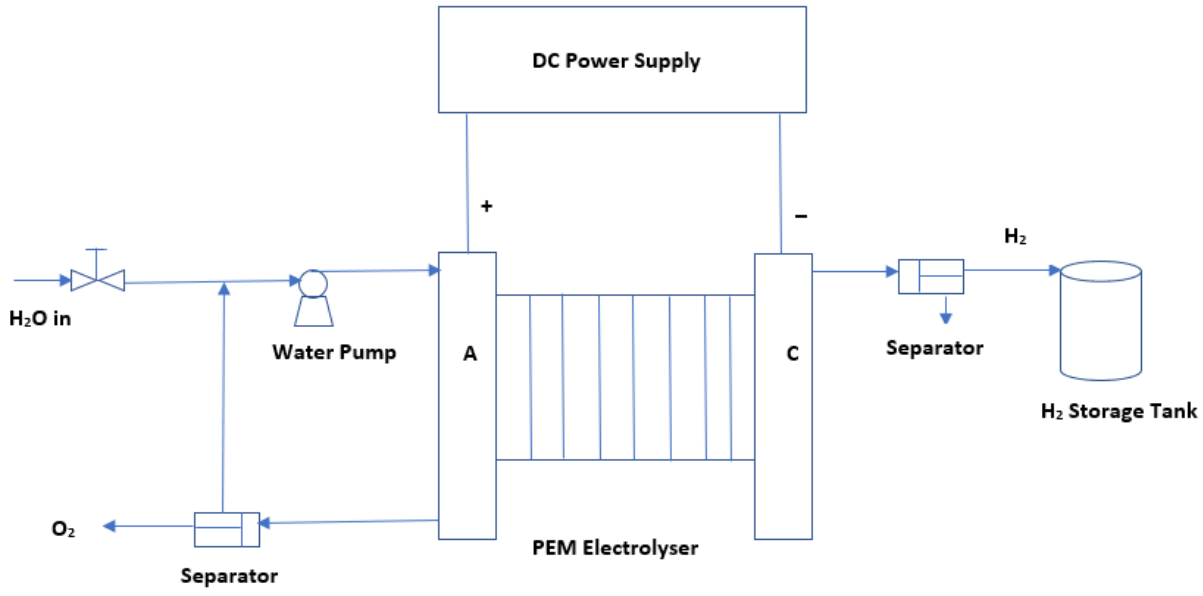

The PEM electrolyzer can be operated under three different modes [2]

1. Atmospheric pressure operation (< 1 standard atmosphere)

2. Differential pressure mode, typically 30 bar to 70 bar.
3. Balanced mode

The differential mode requires the polymer membrane to be thick enough to improve the mechanical stability and decreases gas permeation, which reduces efficiency. It also requires an additional catalyst to re-convert any hydrogen, which, due to higher pressures, would permeate more H_2 back to water.

In balanced mode, there is a similar pressure on the anode and cathode sides. This means the membrane, spacers and porous transport layer can all be thinner given the lower requirement for mechanical strength. This leads to a higher efficiency, since there is less internal cell resistance, but requires capability of the system embodiment to withstand the high pressure.

Most of the simulation studies in the literature show the sensibility studies of cell voltage with current densities at different scenarios. One of the studies considered for model development (Colbertaldo, 2017) includes the sensitivity of hydrogen production (Nm^3/h) vs the electric power input (kW) for the electrolyzer and also the hydrogen production rate(g/h) vs the specific energy consumption (kWh/kg_{H2}). Exhibit 2-11 lists the key design and operating conditions of PEM electrolyzers.

The key variables for the hydrogen injection in NGCC GT are the specific work consumed by the stack for different production rates at various pressure conditions. Mass and Energy balance including the corresponding electrochemical system models that include consideration of Ohmic loss, diffusion loss, activation loss and parasitic losses (short circuits) were included in the model.

Exhibit 2-11 Key Design and Operating conditions of PEM electrolyzer (Colbertaldo, 2017)

	2020-Present	**Target 2050**
Nominal Current Density	1-2 A/cm^2	4-6 A/cm^2
Voltage range	1.4-2.5 V	<1.7 V
Operating temperature	50-60 °C	80 °C
Cell Pressure	<30 bar	>70 bar
H_2 purity	99.9-99.9999%	99.9-99.9999%
Voltage efficiency	50-68%	>80%
Electrical efficiency(stack)	47-66 kWh/kg H_2	< 42 kWh/kg H_2
Electrical efficiency(system)	50-83 kWh/kg H_2	< 45 kWh/kg H_2
Lifetime(stack)	50000-80000 hours	100000-120000 hours
Stack unit size	1MWe	10MWe
Electrode area	1500 cm^2	>10000 cm^2

Exhibits 2-12 and 2-13 compare the input-output model results with the data obtained from the literature (Colbertaldo, 2017). Model results and experimental data compared well.

Exhibit 2-12: Model comparison with data for specific work (kWh_e/kg_{H2}) vs normalized hydrogen production rate at high pressure conditions

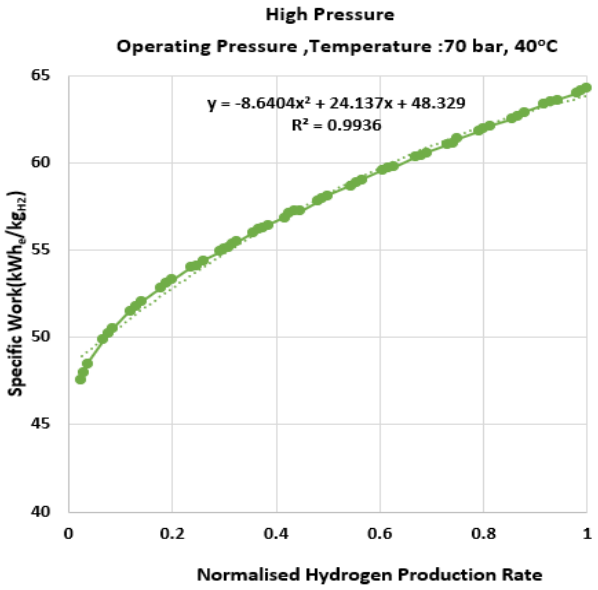

Exhibit 2-13. Model comparison with data for specific work (kWhe/kg H_2) vs normalized hydrogen production rate at medium pressure conditions

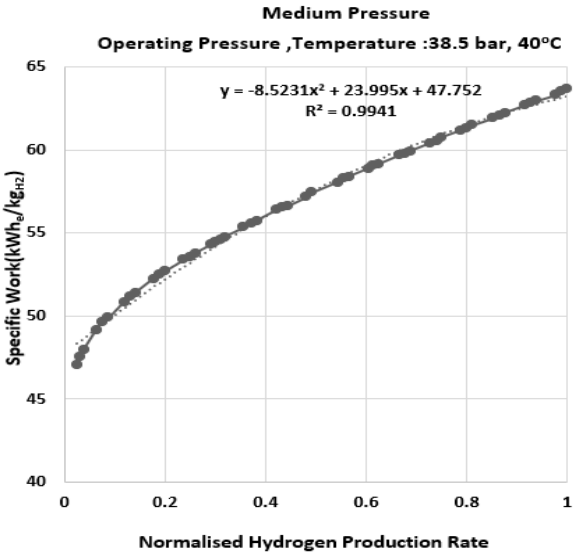

.

In addition to the small scale electrolyzer model described above, additional models were developed for higher capacity hydrogen production. This model was developed from the data of the 250 kWe electrolyzer system at Bright Green Hydrogen's Levenmouth Community energy project at Scotland (Persson et al., 2020). The model considered the losses during stand-by mode, which can play an important role depending on the number of hours the electolyzer needs to idle. The key design and operating conditions are listed in Exhibit 2-14.

Exhibit 2-14 Key design and operating conditions of larger PEM electrolyzer stacks (Persson et al., 2020)

List of Variables	Range of Operation
Power capacity	250 kWe
Current	3050 A
DC voltage	85 V
Volumetric flowrate of hydrogen produced	45 Nm^3/h
No of stack	1
Surface area of individual cells	1500 cm^2
Operating pressure	40 bar
Operating temperature	298 K
Efficiency factor	0.74
Power input at max hydrogen production	176 kWe

In the work of Persson et al. (2020), the data were collected under normal conditions of pressure and temperature (1 atm, 20^{o}C). The maximum power capacity rated at 250 kWe included power needed for the stack, pumps, cooling fans, controls, losses from the receiving transformer and rectifier systems. While the actual power from the plant data showed 176 kWe accounting for other losses encountered in the electrolyzer system. The maximum operating pressure was about 30 bar- a higher pressure helps to conserve the downstream compression cost. A constant temperature operation was assumed for model development.

Exhibits 2-15 and 2-16 compare the model results vs the data for the power input (kW) vs normalized hydrogen production rated at 100 and 250 kWe power. An excellent match can be observed.

Exhibit 2-15: Comparison between the data and model for power input vs normalized hydrogen production rate for a 100 kWe electrolyzer

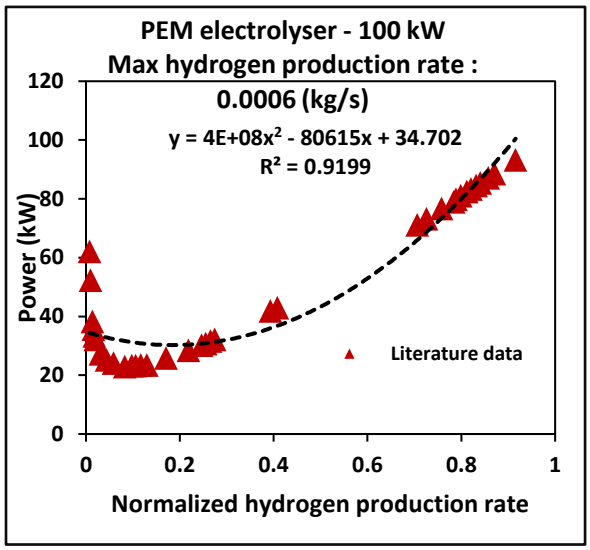

Exhibit 2-16: Comparison between the data and model results for power input vs normalized hydrogen production rate for a 250 kWe electrolyzer

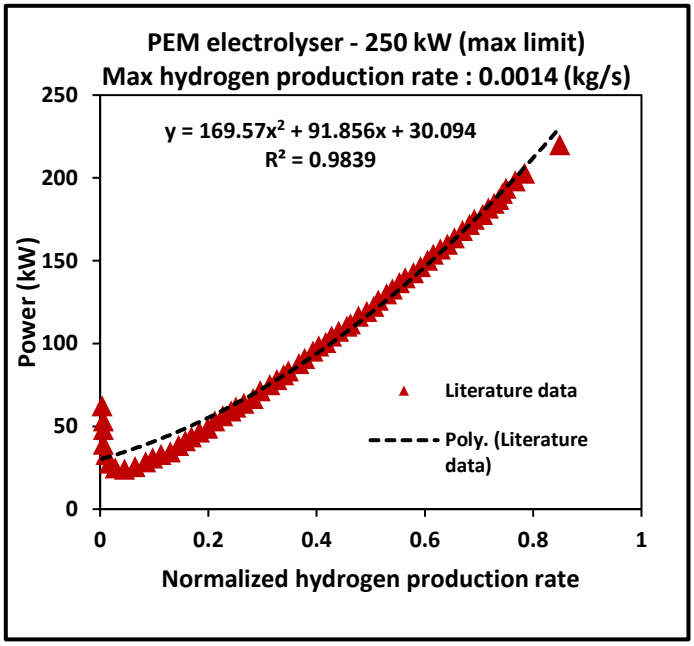

PUMPED HYDRO STORAGE

A diagram of the typical open-loop and closed-loop pumped hydro storage (PHS) is shown in Exhibit 2-37.

Exhibit 2-27. Schematic of the pumped hydro storage (Source: https://www.energy.gov/eere/water/pumped-storage-hydropower)

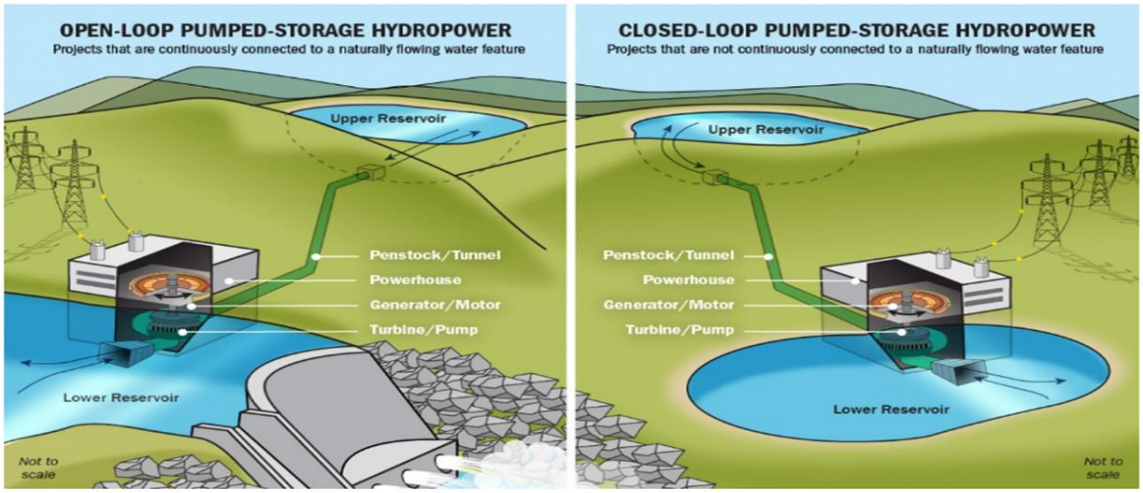

PHS stores and generates energy by transporting water between two reservoirs at different elevations. Energy is stored in the form of gravitational potential energy and converted to electrical energy during demand. During off-peak period, water is pumped from lower reservoir to the higher reservoir (charging), by spinning of the turbines in backward direction, storing the electric energy in the form of hydraulic potential energy. During peak period, water moves down which causes the turbines to spin forward (discharge) generating mechanical energy. The turbine then activates the generators that converts mechanical energy to electricity, satisfying the demand.

A PHS system can be classified as either an open-loop system or a closed-loop system depending on the type of reservoirs used. In an open-loop system, at least one reservoir uses a free-flowing water source to a natural body of water. In contrast, in a closed-loop system, neither reservoir uses/ is connected to, a free-flowing water source. This minimizes the influence on the environment and does not obstruct the natural water flow.

PHS systems offer several advantages such as, flexible start/stop and fast response speed, ability to track and adapt to load changes, can modulate the frequency (Blaabjerg et al. ,2005; Connolly et al., 2010). However, the relatively low energy density of PHS systems requires either a very large body of water or a large variation in reservoir height.

PHS is the only proven largescale (>100 MW (~4100MW)) energy storage technology (Sivakumar et al., 2013). There has been an increased trend of installations and operation of these schemes (Deane et al., 2010). Technically feasible, commercially and socially acceptable site selection is a critical issue for PHS.

The first PHS appeared in 1890s, contained separate pump impellers and turbine generators. In 1950s, a single reversible pump-turbine became available for pumped hydroelectric storage. From 1960's to 1980's there was a significant development of PHS systems, mainly due to the deployment of nuclear power plants (Deane et al., 2010). However, by 1990's the increasing difficulty to identify suitable locations along with the reduced growth of nuclear plants limited the development of PHS. But, in recent years there has been an increasing interest towards PHS as a mature and large-scale energy storage technology to support green energy production. In this context, research is being done on different types of PHS technologies to improve the overall pump-turbine efficiency over a wide range of operating conditions.

Two basic types of PHS are: fixed speed conventional pumped hydro system (C-PHS) and adjustable speed pumped hydro storage (AS-PHS). C-PHS is the traditional technology which utilizes a synchronous electric machine, which allows the unit to operate in both pumping and generating modes by changing the rotational direction of the motor. However, during pumping mode, single speed units are unable to provide frequency regulation. AS-PHS uses a conventional synchronous generator or doubly fed induction machine (DFIM) based on the net operating power. AS-PHS has the advantage to vary the pump and turbine rotation speed for more efficient overall operation and better integration with the power grid. The frequency of the rotor voltage and current can be adjusted to control the speed of the rotor. However, these two models can't operate simultaneously in pumping and generating mode.

A new PHS being developed is the ternary PHS (T-PHS), which can operate simultaneously in HSC mode. A T-PHS unit is typically divided into three parts: a synchronous machine, an exciter to regulate the reactive power or voltage, and a governor to regulate the hydropower or indirectly regulate the electrical power. Despite the advantages, T-PHS incurs high investment costs, high maintenance due to electromechanical complexity, lower efficiency in HSC mode and low stability of the rotating shaft due to low pump submergence.

Each model has its own advantages and disadvantages. In this work a reversible pump turbine unit is modeled to develop a fully working pumped storage system, which is made to follow the load requirements using PID controller for pump and turbine.

The capital cost of PHS vary based on location, installation size, design, etc. As per the US HydroPower market report (2021) from US DOE, typical CAPEX of PHS in 2019 is about $4000-5000/kW. A value of $4500/kW is considered in this project.

LI ION BATTERY STORAGE

Development of the detailed lithium-ion (Li-ion) battery model has been completed in this quarter. In Li-ion battery technology, following reversible reaction takes place:

$$Li \leftrightarrow Li^{+} + e^{-} \tag{2.1}$$

These batteries offer high energy and power densities making them potential candidates for grid level storage (Lawder, 2016).

During charging lithium is deintercalated from the cathode, then diffuses through the electrolyte, and finally intercalates into the active material in the anode. The half-cell redox reactions are:

$$MO_y + Li^+ + e^- \leftrightarrow LiMO_y \tag{2.2}$$

$$LiC_6 \leftrightarrow Li^+ + e^- + C_6 \tag{2.3}$$

Mass balance, liquid phase charge balance, and solid phase charge balance were written for the cathode, anode, and the separator (Lawder, 2016) that is sandwiched between the electrodes for selective transport of Li ions (Northrop et al., 2011). The system of partial differential algebraic equations were solved in Aspen Custom Modeler using method of lines where spatial dimensions are discretized.

Models of three regions- cathode, separator, and anode- are given by Eqs. 2.4-9.

Anode/Cathode

$$\varepsilon_i \frac{\partial c}{\partial t} = \frac{\partial}{\partial x}\left[D_{eff,i}\frac{\partial c}{\partial x}\right] + a_i(1-t_+)j_i \tag{2.4}$$

$$-\sigma_{eff,i}\frac{\partial \varphi_1}{\partial x} - \kappa_{eff,i}\frac{\partial \varphi_2}{\partial x} + \frac{2\kappa_{eff,i}RT}{F}(1-t_+)\frac{\partial \ln c}{\partial x} = I \tag{2.5}$$

$$\frac{\partial}{\partial x}\left[\sigma_{eff,i}\frac{\partial \varphi_1}{\partial x}\right] = a_i F j_i \tag{2.6}$$

$$\frac{\partial c_i^s}{\partial t} = \frac{1}{r^2}\frac{\partial}{\partial r}\left[r^2 D_i^s \frac{\partial c_i^s}{\partial r}\right] \tag{2.7}$$

Separator

$$\varepsilon_s \frac{\partial c}{\partial t} = \frac{\partial}{\partial x}\left[D_{eff,s}\frac{\partial c}{\partial x}\right] \tag{2.8}$$

$$-\kappa_{eff,s}\frac{\partial \varphi_2}{\partial x} + \frac{2\kappa_{eff,s}RT}{F}(1-t_+)\frac{\partial \ln c}{\partial x} = I \tag{2.9}$$

For easier simulation, coordinate transformation was undertaken (Northrop et al., 2011) leading to Eq 2.10-12 corresponding to Eq 2.4-6 and Eq 2.15-16 corresponding to Eq 2.8-9.

To reduce the complexity of the model, a polynomial approximation is developed to simulate the solid phase concentration of Lithium ions resulting in Eq 2.13-14 corresponding to Eq 2.7.

Anode/Cathode

$$\varepsilon_i \frac{\partial c_i}{\partial t} = \frac{1}{l_i}\frac{\partial}{\partial X}\left[\frac{D_{eff,i}}{l_i}\frac{\partial c_i}{\partial X}\right] + a_i(1-t_+)j_i \tag{2.10}$$

$$-\frac{\sigma_{eff,i}}{l_i}\frac{\partial \varphi_{1,i}}{\partial X} - \frac{\kappa_{eff,i}}{l_i}\frac{\partial \varphi_{2,i}}{\partial X} + \frac{2\kappa_{eff,i}RT}{F}\frac{(1-t_+)}{l_i}\frac{\partial \ln c_i}{\partial X} = I \tag{2.11}$$

$$\frac{1}{l_i}\frac{\partial}{\partial X}\left[\frac{\sigma_{eff,i}}{l_i}\frac{\partial \varphi_{1,i}}{\partial X}\right] = a_i F j_i \tag{2.12}$$

$$\frac{\partial}{\partial t} c_i^{s,avg} = -3\frac{j_i}{R_i} \tag{2.13}$$

$$\frac{D_i^s}{R_i}\left(c_i^{s,surf} - c_i^{s,avg}\right) = -\frac{j_i}{5} \tag{2.14}$$

Separator

$$\varepsilon_s \frac{\partial c_s}{\partial t} = \frac{1}{l_s}\frac{\partial}{\partial X}\left[\frac{D_{eff,s}}{l_s}\frac{\partial c_s}{\partial X}\right] \tag{2.15}$$

$$-\frac{\kappa_{eff,s}}{l_s}\frac{\partial \varphi_{2,s}}{\partial X} + \frac{2\kappa_{eff,s}RT}{F}\frac{(1-t_+)}{l_s}\frac{\partial \ln c_s}{\partial X} = I \tag{2.16}$$

Exhibit 2-18 shows comparison of the V-I curve between the model and the literature (Northrop et al., 2011) for 1C discharge rate. It can be observed that the entire profile could be matched well including the limiting current density.

Exhibit 2-18 Comparison of the V-I curve between the model and the literature data (Northrop et al., 2011)

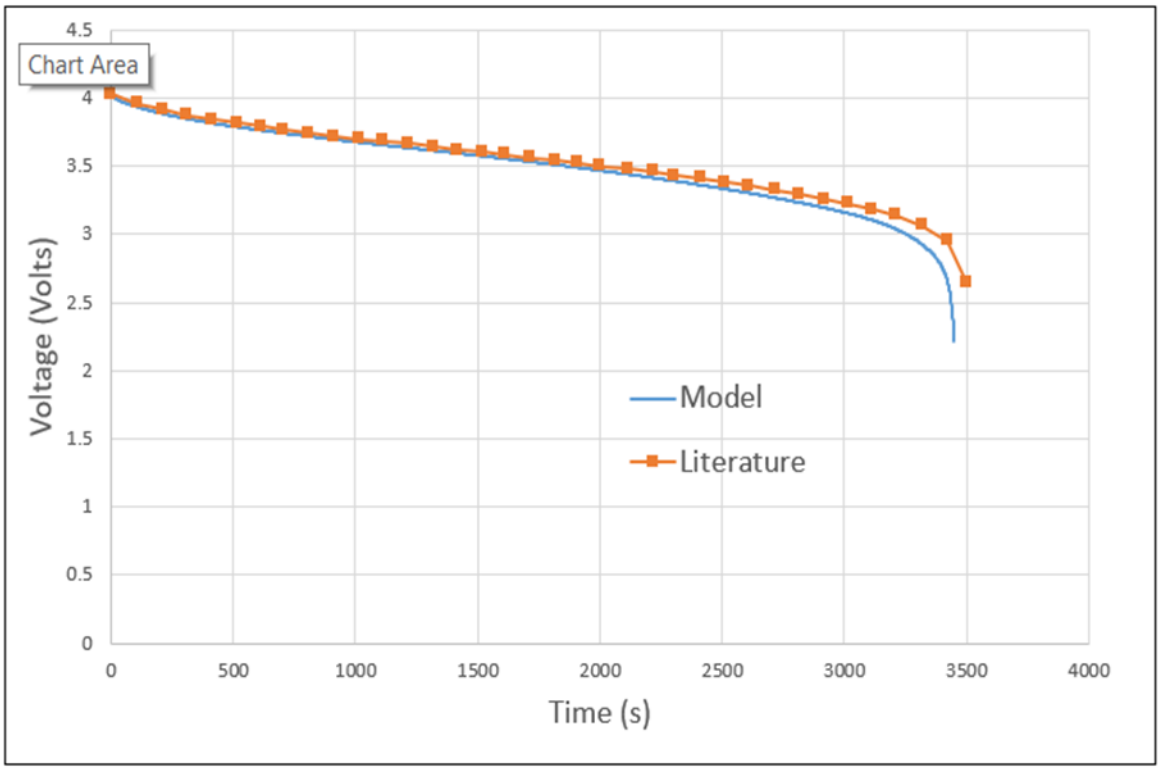

One critical variable for Li-ion batteries is the temporal change of the Li ion concentration profile in the cell. Exhibit 2-19 shows a comparison of the temporal Li-ion concertation profile under 1C discharge at anode/current collector interface, cathode/current collector interface, anode/separator interface, and cathode/separator interface between the model and the literature (Northrop et al., 2011). An excellent match can be observed. It can be observed that the concentration profiles are highly nonlinear. The concentration approaches the maximum concentration at the cathode/separator interface and minimum concentration at the anode/separator interface as the cell state of charge drops below certain value. As the cell state of charge drops, the anode/current collector interface and cathode/collector interface concentration approaches the concentration at the anode/separator interface and cathode/separator interface, respectively, capturing the decreasing concertation gradient in the electrodes with time as expected.

Exhibit 2-19 Comparison of the Li ion concertation profile at the at anode/current collector interface, cathode/current collector interface, anode/separator interface, and cathode/separator interface between the model and the literature data (Northrop et al., 2011)

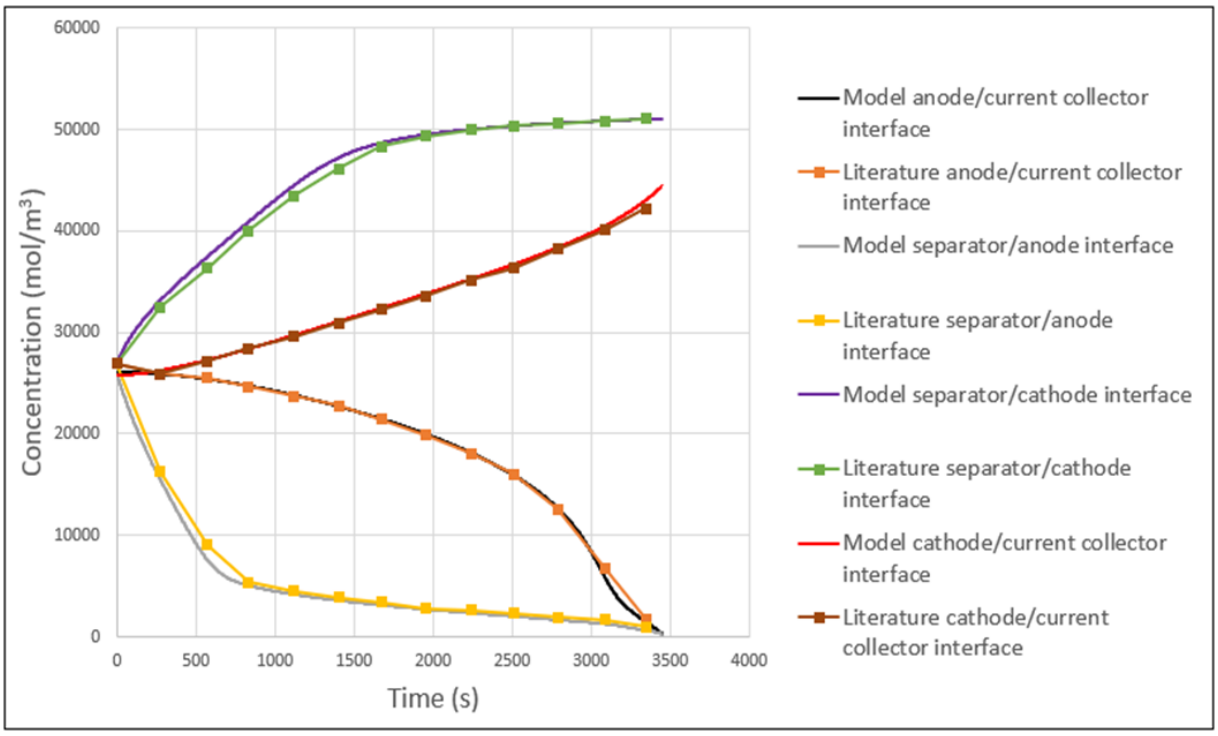

Overall, these results show that the developed Li-ion cell model compared very well with the literature.

SODIUM SULFUR BATTERY STORAGE

A NaS cell consists of a central molten sodium electrode, beta"-alumina solid ceramic electrolyte, and an outer molten sulfur/sodium-polysulfide electrode as shown in Exhibit 2-20.
The half-cell reactions that take place in the sodium and sulfur electrodes, respectively, are given by:

$$2Na \leftrightarrow 2Na^{+} + 2e^{-} \quad (2.17)$$

$$2Na^{+} + xS + 2e^{-} \leftrightarrow Na_2S_x \quad (2.18)$$

The overall cell reaction is given by:

$$2Na + xS \leftrightarrow Na_2S_x \quad (2.19)$$

where *x* is the variable subscript for sulfur in the sodium-polysulfide melt. The forward reaction takes place during cell discharge when the positive sodium ions move from the anode to the cathode through the beta"-alumina electrolyte. The beta"-alumina electrolyte is practically impermeable to electrons. Sodium ions react with the liquid sulfur in the cathode to produce sodium polysulfides. Under fully charged condition, the sulfur electrode contains only sulfur. As discharge operation begins, the sulfur electrode transitions to a two-phase mixture of sulfur and polysulfide. As the reaction progresses, more sodium ions react with the sulfur and the mole fraction of total sulfur decreases, transitioning into single-phase region with only sodium-polysulfide melt. Composition of the sulfur electrode changes based on the amount of sodium that crosses the electrolyte. The phase of the melt changes depending on the SOD of the cell since 'x' changes depending on the SOD.

Exhibit 2-20: Schematic of a central sodium sulfur cell

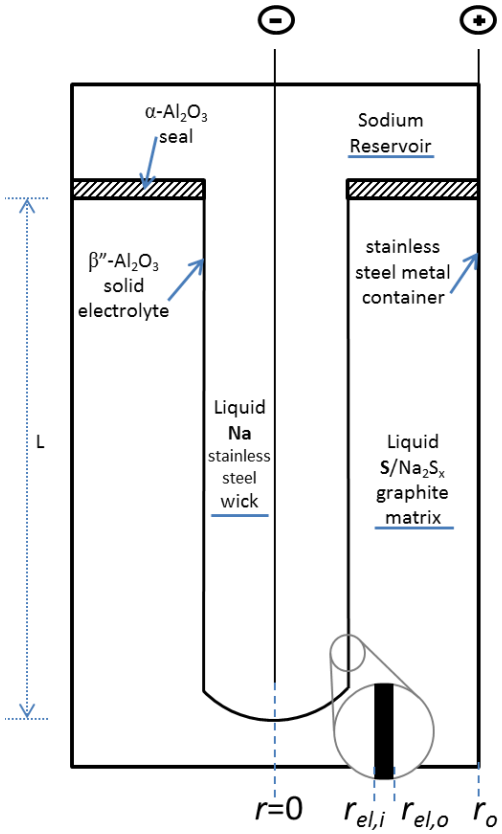

A first principles, fully coupled thermal-electrochemical dynamic model (Schaefer et al., 2020) of the entire sodium-sulfur cell was developed in Aspen Custom Modeler V.8.4. The model results were compared with the experimental data (Kawamoto and Kusakabe, 1989). Exhibit 2-21 shows that the model results compare well with the literature data for both cell voltage and temperature.

Exhibit 2-21: Comparison between our model and the experimental data for NaS cell voltage and temperature (Kawamoto and Kusakabe, 1989)

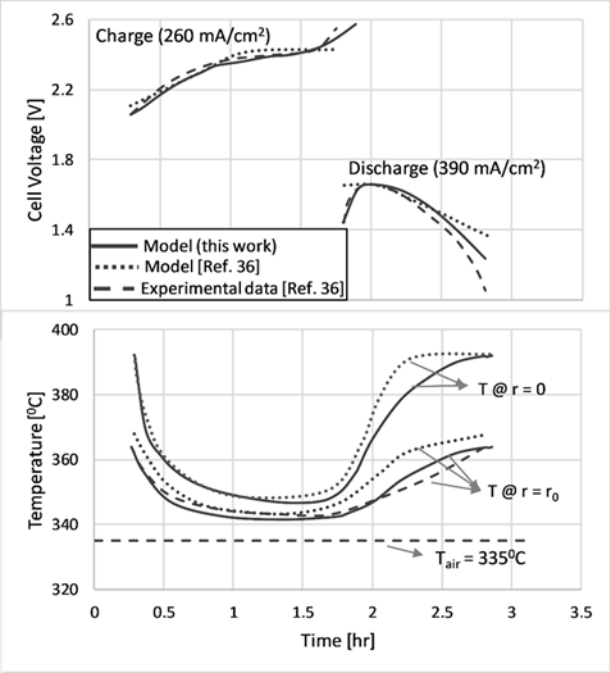

VANADIUM REDOX FLOW BATTERY STORAGE

Redox flow batteries (RFBs) have gained increased interest in energy storage Because of the high energy efficiency, safety, low cost and long cycle life (Lourenssen et al., 2019). Moreover, RFBs have flexible design, because of the advantage of the independency in energy capacity and power generation. Of all the available RFBs, vanadium redox flow battery (VRFB) system is the most innovative and commercially available battery. Compared to other RFBs such as Zn-Br, Fe-Cr and Zn-air batteries, VRFBs have advantages like (a) unlimited energy capacity - by increasing the quantity of electrolyte, VRFB can supply almost unlimited amount of energy, (b) it can be left completely discharged for long periods with detrimental effect, (c) no permanent damage is caused by accidental mixing of electrolytes, (d) the electrolyte is aqueous and essentially safe and non-flammable (Gu et al., 2020). Moreover, in VRFB, the ability of vanadium to exist in different oxidation states is exploited and same element is used in both cathode and anode, which avoids cross-contamination of elements making it environmentally friendly (Yuan et al., 2019). VRFBs have an overall efficiency of 70-90% with a lifetime of more than 15,000 – 20,000 charge/discharge cycles (Gu et al., 2020).

The vanadium redox flow battery considered in this study consists of an ion-exchange membrane, separating the positive electrode and negative electrode as shown in Exhibit 2-22. The system contains two tanks and two pumps connected to the negative electrode and positive electrode respectively, for the electrolyte flow. This separation of the energy conversion part and the storage part helps in having decoupled energy and power capacity.

The half-cell reactions that take place in the positive and negative electrodes, respectively, are given by:

$$VO^{+2} + H_2O \leftrightarrow VO_2{}^{+} + 2H^{+} + e^{-} \qquad E^0 = 1.00V \quad (2.20)$$

$$V^{+3} + e^{-} \leftrightarrow V^{+2} \qquad E^0 = -0.26V \quad (2.21)$$

The forward reaction takes place during charging when V^{+3} and V^{+4} ions enter the cell. V^{+4} is oxidized to V^{+5} by releasing an electron which is removed by a conducting electrode material and a hydronium ion which moves across the membrane. At the anode, the electron reduces V^{+3} to V^{+2} and the hydronium ion offsets the overall charge of the half-cell. The ions leave the cell in charged state, as V^{+5} and V^{+2}. The reverse of charging occurs during discharge.

The overall cell reaction is given by:

$$VO^{+2} + H_2O + V^{+3} \leftrightarrow VO_2{}^{+} + 2H^{+} + V^{+2} \qquad E^0 = 1.25V \quad (2.22)$$

Along with the half-cell reactions a number of other reactions take place within the cell, which reduces the capacity of the cell subsequently. The following crossover reactions occur due to the transport of vanadium ions through the membrane:

Negative electrode:

$$VO^{+2} + V^{+2} + 2H^{+} \rightarrow 2V^{+3} + H_2O \quad (2.23)$$

$$VO_2{}^{+} + 2V^{+2} + 4H^{+} \rightarrow 3V^{+3} + 2H_2O \quad (2.24)$$

Positive electrode:

$$V^{+2} + 2VO_2{}^{+} + 2H^{+} \rightarrow 3VO^{+2} + H_2O \quad (2.25)$$

$$V^{+3} + VO_2{}^{+} \rightarrow 2VO^{+2} \quad (2.26)$$

Gaseous side reactions notably, the evolution of oxygen at the positive electrode and evolution of hydrogen at negative electrode takes place.

$$2H_2O \leftrightarrow O_2 + 4e^{-} + 4H^{+} \quad (2.27)$$

$$2H^{+} + 2e^{-} \leftrightarrow H_2 \quad (2.28)$$

Along with these ion-crossover and side reactions, water transport through the membrane causes membrane degradation. A first-principles model of this system was developed at WVU (Vudata and Bhattacharyya, 2022). The results from the model including all leading capacity fading mechanisms were found to compare well with the literature.

Exhibit 2-22: Schematic of the Vanadium Redox Flow Battery

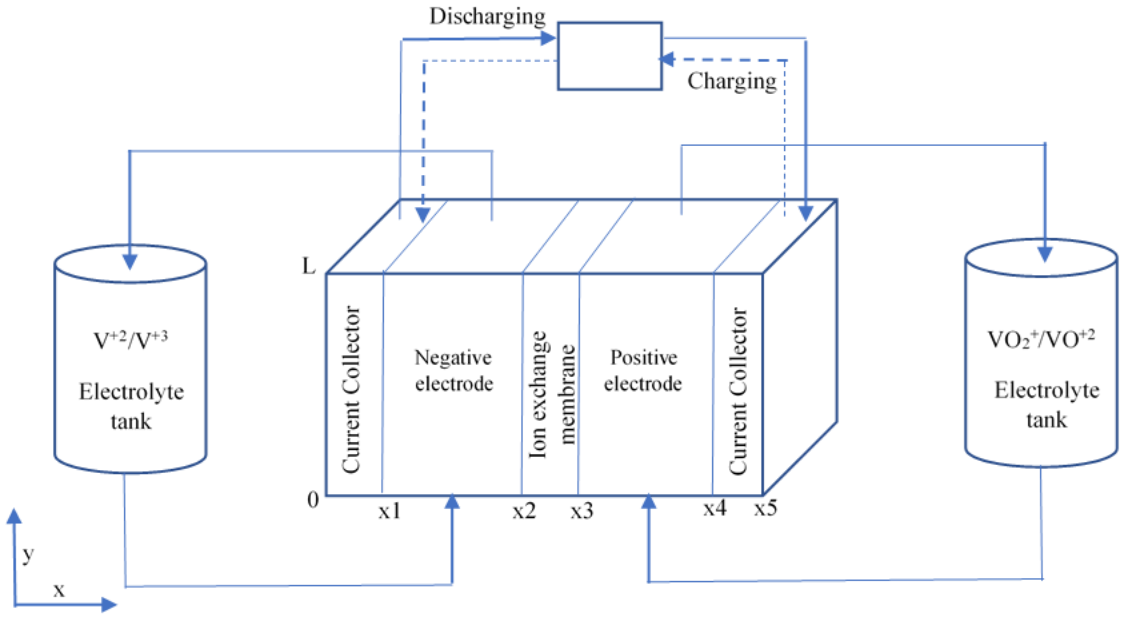

Due to the difference in valances, the ionic potential at the positive electrode is less when compared to the negative electrode. The effect of Donnan potential drops the ionic potential at the membrane electrode interfaces compared to the electrode ionic potential. This drop satisfies the equivalent trivial ionic potential at the interface, where the potential is discontinuous. The positive side has higher proton and bi-sulphate concentrations than the negative side, because of the higher valence of the cations in the negative electrolyte compared to positive electrolyte. The proton diffusion towards the negative side is balanced by the electro-migration flux. The concentration profile for HSO_4^-, V^{+2} and V^{+3} are convex and concave for H^+, V^{+4} and V^{+5} in the membrane. There is an accumulation of vanadium ions in the positive side as the cell keeps cycling. This is because of the imbalance in the net flux during charging and discharging. The side reactions, ion-crossover reactions and water transfer does not affect the profile of the vanadium ion or ion potential.

It was observed that cell voltage profile can change considerably depending on the current density, electrolyte flow rate and whether the cell is charging or discharging. The cell voltage profile was observed to increase during charge and decrease during discharge. It was observed that as the current density is increased, cell voltage can decrease or increase if the cell is charging or discharging. If the electrolyte flowrate is increased keeping the current density constant, the cell voltage decreases during charging and increases during discharging. It was observed that as

the tank volume increases, the time taken to charge/discharge increases as expected for a given current density.

3 REDUCED ORDER MODEL DEVELOPMENT

PROCESS DESCRIPTION

Reduced order models (ROMs) of several systems are developed for computational tractability of the large-scale optimization problem as well as to handle the issue with software compatibility.

ROM of the NGCC Plant

The dynamic model of NGCC plant was developed in Aspen Plus Dynamics (APD). This model has high fidelity, but also has high computational cost. Therefore, a ROM of the NGCC plant with acceptable accuracy and computational efficiency is required for optimization.

Based on the high-fidelity dynamic model, the linear multiple-input-multiple-output (MIMO) state-space model of the NGCC plant was first generated using the Control Design Interface (CDI) tool in APD. That linear model, denoted as full order model (FOM) in this report, also has large number of states and therefore further reduction is desired. Balanced truncation method was used to eliminate the weakly coupled states and generate the ROM on the basis of Hankel singular value (HSV) decomposition.

The number of inputs is based on those that are used as decision variables or specified inputs in optimization while the outputs are those that are used directly or indirectly for cost calculation and or those that are used as input for subsequent inputs and/or those that are used as constraints during optimization. Storage technologies can be standalone or integrated. Standalone storage technologies include pumped hydro, vanadium redox flow battery and Li-ion battery while other technologies are integrated. For each integrated storage technology, a separate ROM of the NGCC plant was developed that includes the additional inputs and/or outputs corresponding to the storage. For example, for compressed air energy storage (CAES), additional inputs include the air injection flowrate and temperature and pressure while the outputs are extraction air flowrate, temperature, and pressure.

Exhibit 3-1 shows step changes in H_2 flowrate and natural gas (NG) flowrate that are simulated to test the ROM of the NGCC plant with H_2 injection. Exhibit 3-2 shows comparison of APD, FOM, and ROM for net power output from the NGCC plant and high pressure (HP) steam flowrate to the ST. It is observed that results from APD, FOM, and ROM compare well.

Exhibit 3-3. Step Changes in H_2 flowrate and NG flowrate for testing the ROM of the NGCC plant with H_2 Injection

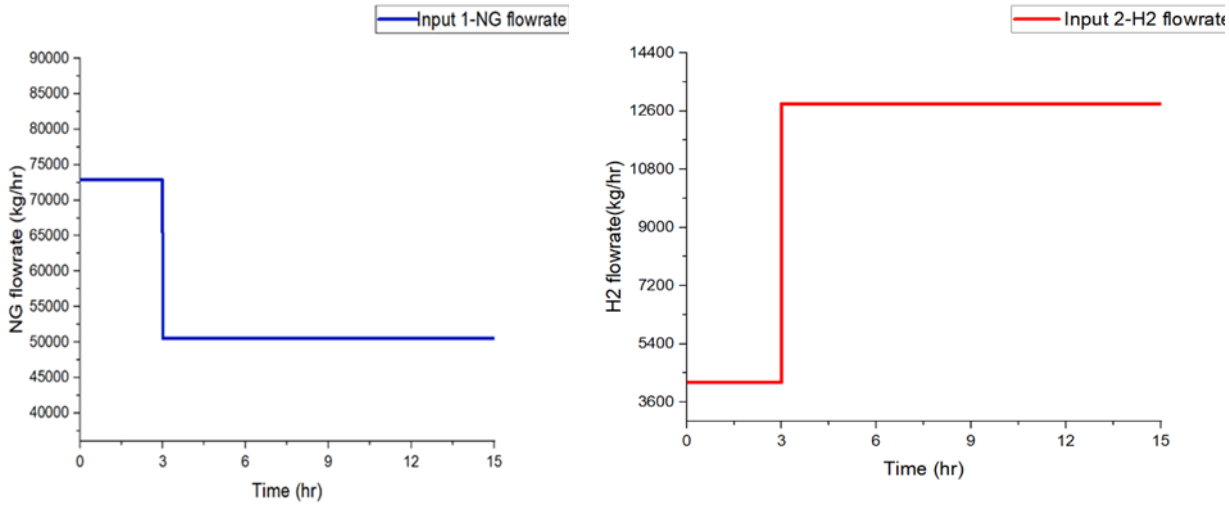

Exhibit 3-2. Comparison of APD, FOM and ROM of net power output and HP steam flowrate for the NGCC Plant with H_2 Injection

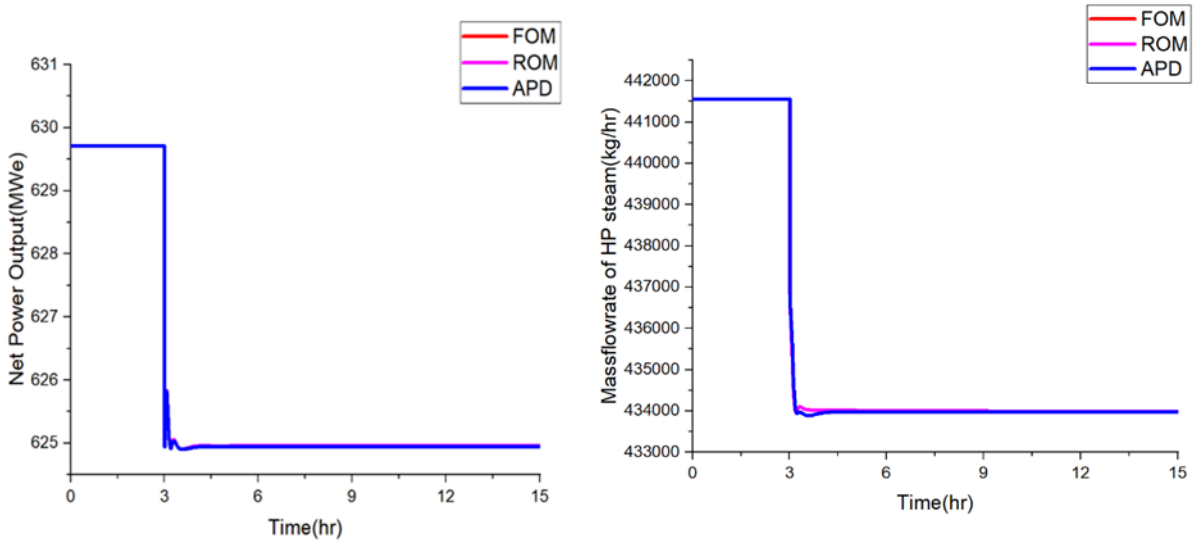

ROM of CES

To generate reduced order models for the CES system, we generated data from several simulations with optimal process configuration as determined in the previous quarter. The optimal process flowsheet was then used to generate surrogate on the power and energy stored as a function of the state variable (mass of air) and the flowrate of air. These expressions were then used for the optimal scheduling of the power plant to make operational decisions of

charging and discharging.

From several simulations done on the optimal design, functions are obtained for charging and discharging in the CES system. Note that all these simulations are ASPEN simulations wherein detailed thermodynamics along with process detail of cold storage have been adhered to.

Cost expressions are complex functions of the design capacity of power and energy. These functions are highly complex to obtain from individual equipment level scaling. Thus, to obtain these we used a systems approach and split the process as three systems: charging, storage, and discharging. This allowed us to scale the necessary equipment on the charging and discharging side for meeting power requirements of the design and the energy storage can be designed based on the energy (MWh) of the rated design. These cost expressions were also obtained from several simulations and are fitted using the power law.

The surrogate model for HTTS including the power ($P_{i,t}^{S}$) and energy ($E_{i,t}$) function based on the mass of molten salt in hot storage tank (defined as the state variable $s_{i,t}$) , and the molten salt flow rate (defined as the flow variable $l_{i,t}$). Q_c is the charging heating rate. W_d is the power generated per one unit of steam. R_f is the ratio of discharging steam and molten salt flow rate

$$\boldsymbol{P_{i,t}^{S} = -z_{i,t,b=c}^{op}\, Q_c\, l_{i,t} + z_{i,t,b=d}^{op} W_d\, R^F l_{i,t}} \qquad (3.1)$$

$$\boldsymbol{E_{i,t} = W_d R^F s_{i,t}}$$

The total investment cost ($C_i^{S,iv}$) consists of reheater (R), steam generator package (B) (including boiler, preheater, deaerator and condenser) , storage tank (t), molten salt pump (pp) as well as the storage medium (u_{ms}) cost. The fixed variable cost($C_i^{S,of}$) is 5% of the total investment cost per year. The total variable cost based on operating cost of power block ($4.7/kwh).

$$\boldsymbol{C_i^{S,iv} = C_1\left(a_B F^{max b_B} + a_{RH}\, F^{max b_{RH}} + a_{tk} M^{tot b_{tk}} + a_{pp}\, F^{max b_{pp}} + u_{ms} M^{tot}\right)}$$

$$\boldsymbol{C_i^{S,of} = C_2\, C_i^{S,iv}} \qquad (3.2)$$

$$\boldsymbol{C_{i,t}^{S,ov} = u_{Power\ Block} P_{i,t}^{S}}$$

ROM of NaS Battery

Using the data generated in this model, input-output models are identified.

For model identification, all the models are linear in parameter (LIP) models. A LIP model is written as:

$$y(k) = \varphi(k) H \qquad (3.3)$$

where $y(k)$ is the output at time instant k, $\varphi(k)$ is the regression vector, and H is the parameter vector. Least squares estimate for parameter vector H is:

$$H = (\varphi^T \varphi)^{-1} \varphi^T Y \qquad (3.4)$$

In this work, the NAARX (nonlinear additive autoregressive with exogenous input) model (Bhattacharyya and Rengaswamy, 2010) is considered as the nonlinear LIP model, which is given as:

$$y(k) = \sum_{i=0}^{n} H_1(i,p)u(k-i)^p + \sum_{j=1}^{r} H_2(j,q)y(k-j)^q\,, \quad p = 1{:}P, q = 1{:}Q \quad (3.5)$$

Where H_1 is the parameter vector of the previous time step input (i.e input at time (k-1)) and H_2 is the parameter vector of the previous time step output (i.e output at time (k-1)). Input memory n and p, and output memory r and q are determined by akaike information criterion (AIC).

AIC has been used in this work as a testing criterion for selecting statistical models. AIC gives a good fit, but at the same time penalizes increased number of estimated parameters thereby discouraging overfitting. AIC is given by:

$$AIC = Nln\left(\frac{TSE}{N}\right) + 2K \quad (3.6)$$

where N is the number of data points, TSE is the total squared error, and K is the number of fitted parameters. Until the AIC value changes significantly, model complexity of a given form will be increasing. When there is no significant difference in AIC between two models, then the simpler model is chosen.

Based on direction of power flow and state of sulfur electrode, four models were generated: two in charging phase and two in discharging phase for respective phases. Current and air velocity are considered as decision variables/ model inputs. Cell voltage, power, air temperature, air mass flowrate and SOD are the model outputs. During discharging in two-phase region, for the inputs, the model was validated as shown in Exhibit 3-3.

Exhibit 3-3: Performance of the discharging model in two-phase region corresponding to simultaneous current and air velocity

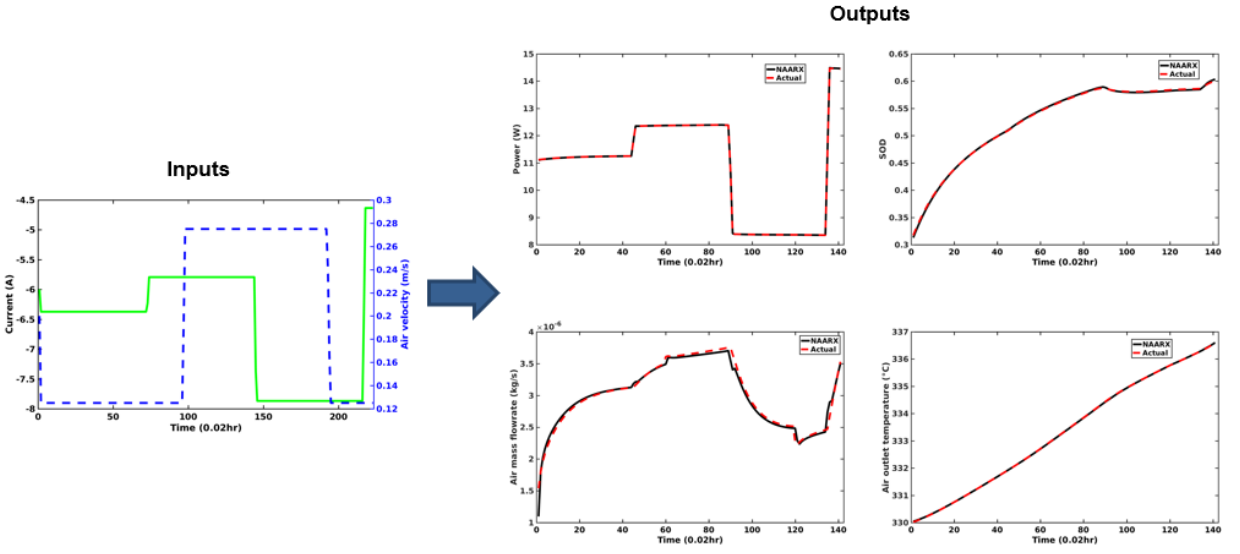

4 DOWNSELECTION

METHODOLOGY

A general optimization framework was developed for the downselection problem and was embedded this in the back-end of a software prototype named "THESEUS" (**T**ec**H**no-**E**conomic framework for **S**ystematic **E**nergy Storage **U**tilization and down**S**election). The overall formulation which forms the back-end framework of THESEUS is given below:

$$\min TC = \sum_{i=1}^{NI}\left(C_i^{S,iv} + C_i^{S,of} + \sum_{t=1}^{NT}\left(C_{i,t}^{S,ov} + C_{i,t}^{FP,ov}\right) + C_t^{FP,rc} + C^{os} + C^{us}\right) \quad (4.1a)$$

$$P_t^{dem} = \sum_i P_{i,t}^S + P_t^{fp} - P_t^{os} + P_t^{us} \quad (4.1b)$$

$$C^{os} = \sum_t P_t^{os} SC^{os} \Delta \mathrm{t} \quad (4.1c)$$

$$C^{us} = \sum_t P_t^{us} SC^{us} \Delta \mathrm{t} \quad (4.1d)$$

$$|P_{t+1}^{FP} - P_t^{FP}| \le ro^{FP} P^{FP,nom} \Delta t \quad (4.1e)$$

$$\eta_t^{FP} = f3(P_t^{FP}) \quad (4.1f)$$

$$P^{FP,nom} lf^{FP,min} \le P_t^{FP} \le P^{FP,nom} \quad (4.1g)$$

$$C_t^{ov,FP} = c4\, P_t^{FP} \frac{\eta^{FP,nom}}{\eta_t^{FP}} \quad (4.1h)$$

$$C_t^{rc,FP} = c5|P_{t+1}^{FP} - P_t^{FP}| \quad (4.1i)$$

$$P_{i,t}^S = f1_i\left(s_{i,t},\, l_{i,t},\, z_{i,t}^b,\, x_i\right) \quad (4.1j)$$

$$E_{i,t} = f2_i(s_{i,t}) \quad (4.1k)$$

$$-z_{i,t}^C P_{i,t}^S \le y_i P_i^{max,C} \quad (4.1l)$$

$$z_{i,t}^D P_{i,t}^S \le y_i P_i^{max,D} \quad (4.1m)$$

$$E_{i,t+1} = E_{i,t} - P_{i,t}^S \Delta t \quad (4.1n)$$

$$E_{i,t=NT+1} = E_{i,t=1} \quad (4.1o)$$

$$z_{i,t}^{idle} + z_{i,t}^C + z_{i,t}^D = 1 \quad (4.1p)$$

$$0 \le x_i \le E_i^{max} y_i \quad (4.1q)$$

$$0 \le E_{i,t} \le x_i \quad (4.1r)$$

$$C_i^{S,iv} = c1_i(x_i) CRF_i \frac{T}{8760} \quad (4.1s)$$

$$C_i^{S,of} = c2_i\,(P_i^{max}) \frac{T}{8760} \quad (4.1t)$$

$$C_{i,t}^{S,ov} = c3_i(P_{i,t}^S) \quad (4.1u)$$

Here, the optimization objective represented by Eq. 4.1a represents the minimization of the integrated system cost. We defined 3 distinct set of constraints: the grid-level constraints, the power plant model and energy storage model. Eqs. 4.1b-4.1c represent the grid-level constraints and denote the overall energy balance and the electricity oversupply/undersupply cost penalty.

Eqs. 4.1e-4.1i represent the power plant model, with Eqs. 4.1e-4.1g denoting the general operational model and Eqs. 4.1h-4.1i denoting the general cost model. Furthermore, Eqs. 4.1j-4.1u denote the storage model, with Eqs. 4.1j-4.1k representing the technology-specific models in terms of the storage state variable $s_{i,t}$, storage flow variable $l_{i,t}$, storage operational state $z_{i,t}^{b}$, and storage design x_i. Eqs. 4.1l-4.1r represent the general operational model of each storage technology, while Eqs. 4.1s-4.1u denote the general cost models. This overall framework forms the back-end of THESEUS and is first tested for individual technology integration considering cryogenic energy storage (CES), molten salt thermal storage (HTTS) and compressed air energy storage (CAES), in addition to the NaS battery storage previously considered. This framework is demonstrated for an NGCC plant with 641 MW nominal capacity to determine optimal storage technology, size and operation.

RESULTS

For generating the results, we first considered a nominal net demand profile with increasing levels of demand variability. The corresponding levelized cost of storage (LCOS) for all the 9 considered storage technologies for the case of integration with NGCC power plants is shown in Exhibit 4-1. We find that the optimal rank order of storage technologies determined by the LCOS shows variation with increasing demand variability. Overall, mechanical energy storage in the form of compressed air energy storage (CAES) is found to be the most cost-effective technology to mitigate the net demand fluctuations across all demand scenarios. NaS battery exhibits the highest LCOS for 20% and 40% demand variability increase levels, while VRFB is the most expensive technology for higher levels of demand variability. We also find that PHS is more expensive than Li-ion battery for low variability in demand. However, PHS becomes more economical for high demand variability levels when long energy duration is required.

Exhibit 4-1: LCOS of the 9 candidate storage technologies for increasing demand variability levels

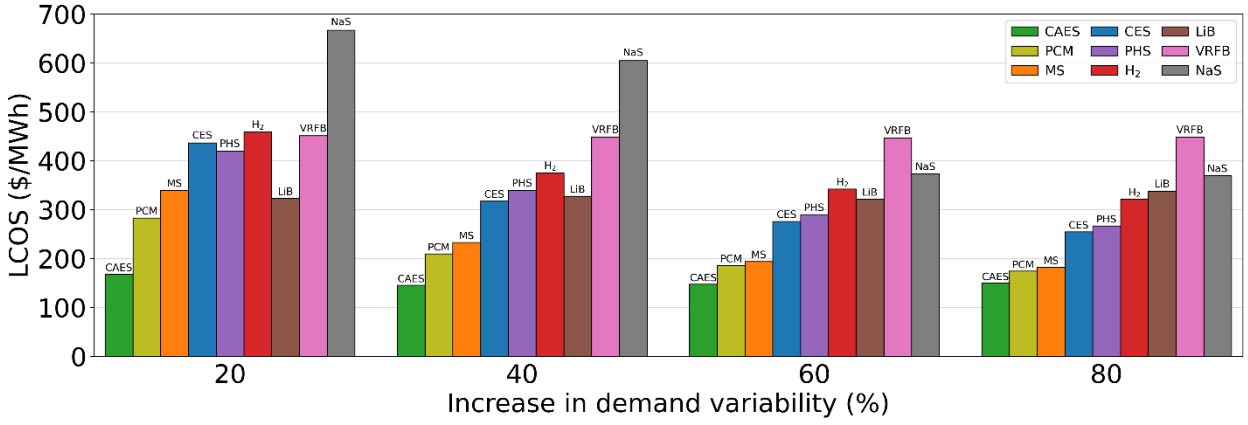

We further extended the analysis to consider different demand profiles in a year. Exhibit 4-2a shows the net demand data for 2021 for the entire state of California. Exhibit 4-2b shows the

corresponding scaled net demand profiles for the fossil plant with 40% increase in the demand variability. To enable computational tractability in optimization, 50 representative profiles are selected from the 365 days of demand data.

Exhibit 4-2a: Statewide net demand data for California in 2021

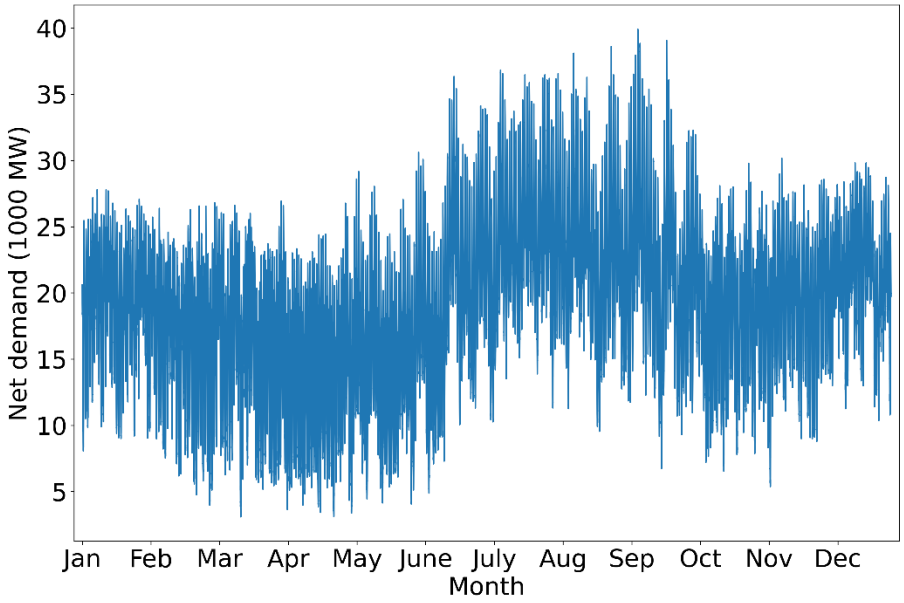

Exhibit 4-2b: Scaled daily net demand profiles for the NGCC power plant

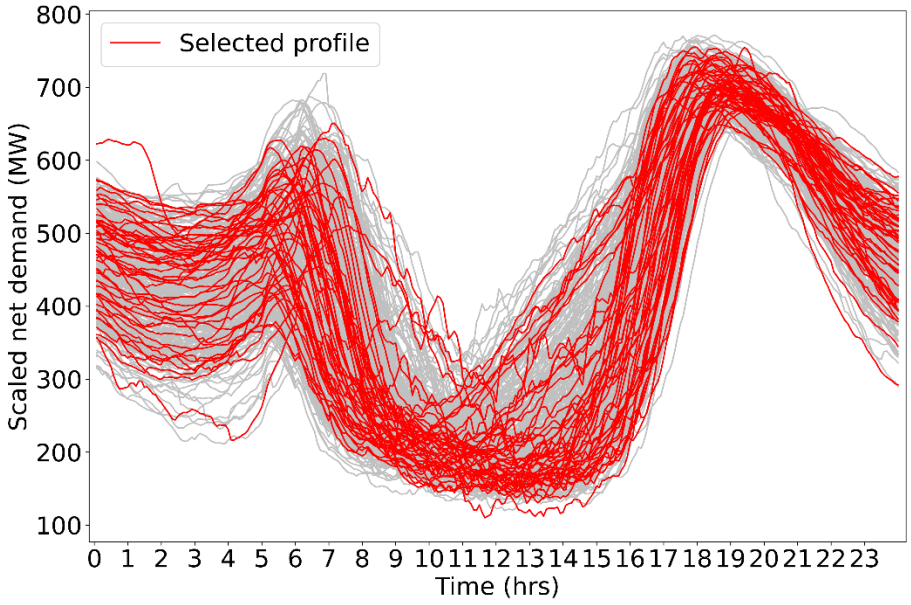

Again, we observed that it is optimal to integrate energy storage with the NGCC power plant to reduce the electricity oversupply and undersupply to the grid and avoid the resulting penalties. Exhibit 4-3 depicts the variation of the optimal LCOS and integration size of the 9 energy storage

technologies across the 50 demand scenarios. In Exhibits 4-3a and 4-3b, the energy storage technologies are arranged in the ascending order of the average LCOS and size, respectively. Similar to our previous observation, we found that CAES has the lowest average LCOS over all the demand scenarios, while NaS battery is the most expensive technology with the highest average LCOS. On the other hand, hydrogen storage exhibited the lowest average integration size, while the battery technologies i.e., Li-ion and NaS batteries, and PHS have large integration sizes. Due to the limits on the battery voltage and state of charge (SOC) and state of discharge (SOD), the utilization of the battery technologies was less than 100% which increases the battery integration size.

Exhibit 4-3a: LCOS for the 50 selected demand profiles

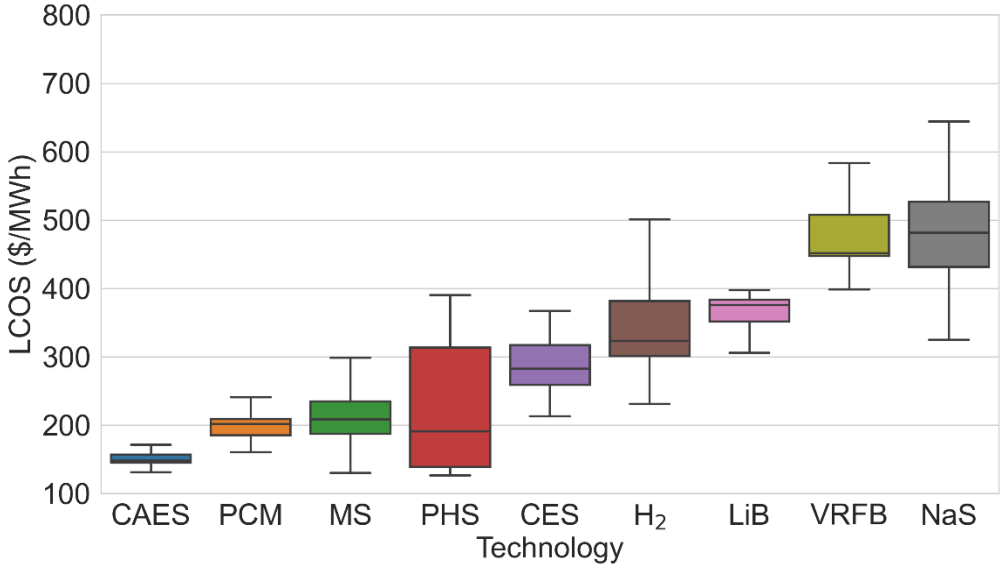

Figure 4-3b: Energy storage integration size for the 50 selected demand profiles

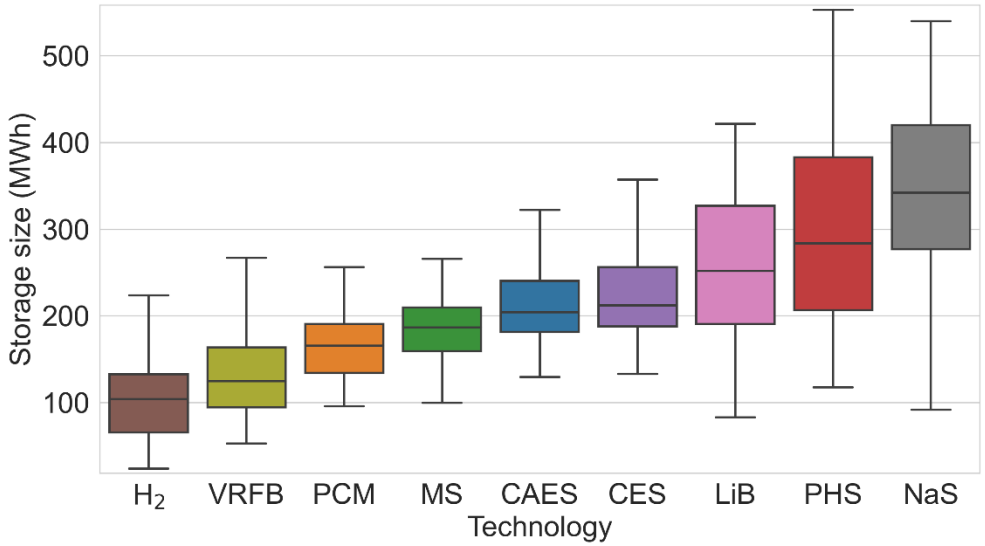

Next, we investigated which storage technology is the most optimal for the decentralized integration. The most cost-effective technology for a given demand scenario was identified as the technology with the lowest LCOS. Although we see from Exhibit 4-3a that CAES was the storage technology with the lowest average LCOS, the best integration technology varied depending on the demand profile. CAES was found to be the best technology for 31 out of the 50 demand profiles, whereas PHS was the most optimal storage technology for the remaining 19 demand scenarios. Exhibits 4-4a and 4-4b show the net demand profiles for which CAES and PHS are the most optimal storage technologies, respectively. The demand profiles for which PHS was the best technology have a distinct band of low net demand during the day. Overall, we found that for demand profiles with CAES as the best integration technology, the net demand is less than the minimum turndown capacity of the NGCC power plant for an average of 4.9 hours. Conversely, the average duration for which the net demand was less than the minimum NGCC capacity was 7.3 hours for cases when PHS is the best-suited technology. Thus, PHS is the most optimal storage technology for integration with the NGCC power plant for cases when long duration energy storage is required.

Exhibit 4-4a: Demand profiles for which CAES has the lowest LCOS

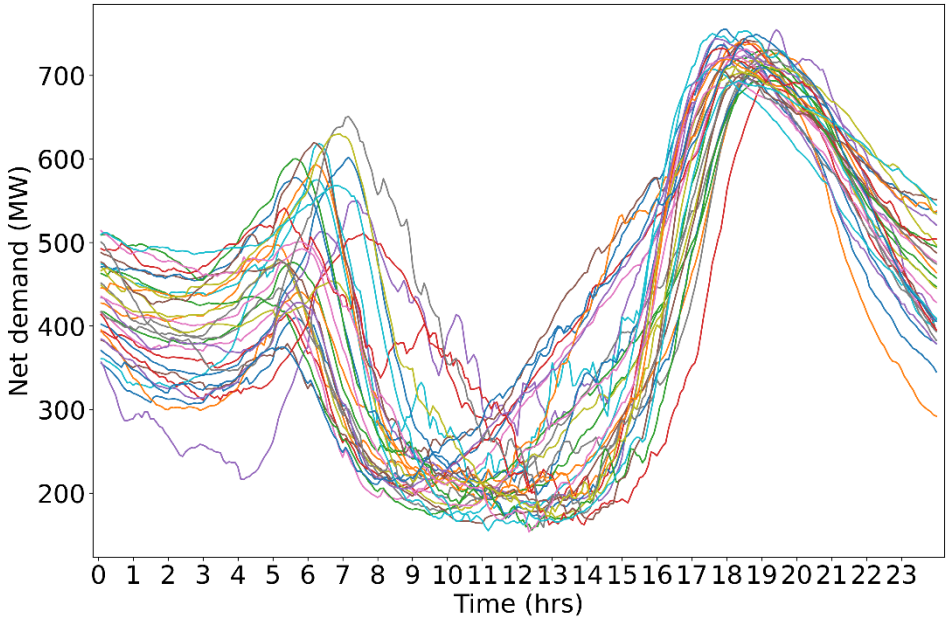

Figure 4-4b: Demand profiles for which PHS has the lowest LCOS

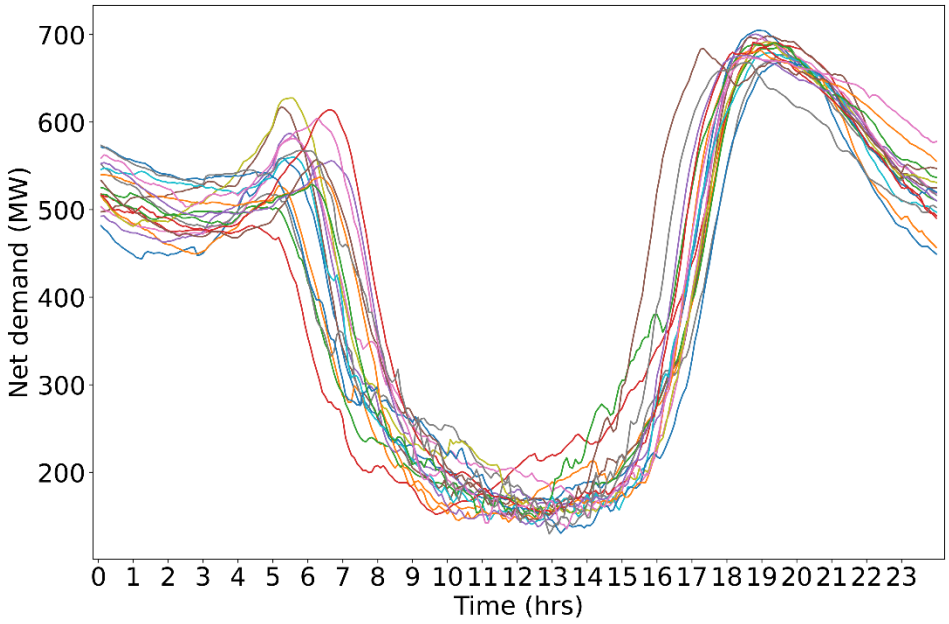

We further studied scenarios where the battery technologies are better than other types of storage technologies. Exhibit 4-3a shows that the battery technologies rank at the bottom of the order when the average LCOS is considered. However, we also found that for 22 out of the 31 demand scenarios with CAES as the best storage technology, the Li-ion technology had lower LCOS than mechanical (PHS) storage, chemical (H_2) storage and thermal (CES) storage. For these demand scenarios, the average ramping requirement was 8% higher than the cases when the Li-ion battery had higher LCOS. Furthermore, the average duration for which the net demand was less than the NGCC minimum capacity during the day is 40% lower. This indicates that compared to PHS, H_2 and CES systems, Li-ion battery was best-suited to mitigate the intermittency of renewable energy and manage the demand fluctuations for profiles with larger ramping and shorter storage duration requirements.

For the case of energy storage integration with SCPC power plants, we found that the storage LCOS is on an average higher than the LCOS of storage integration with NGCC power plants. This is shown in Exhibit 4-5a. This is due to the higher power generation cost of SCPC power plants, which increases the charging cost of energy storage, and thereby the LCOS. The optimal ranking of the storage technologies indicates that CAES is the most cost-effective technology for the integration and the battery technologies are the most expensive. However, PHS now ranks as the second-best technology compared to its rank 4 for the NGCC integration case.

Exhibit 4-5: Comparison of (a) average LCOS and (b) average storage size for integration of energy storage with NGCC and SCPC power plants

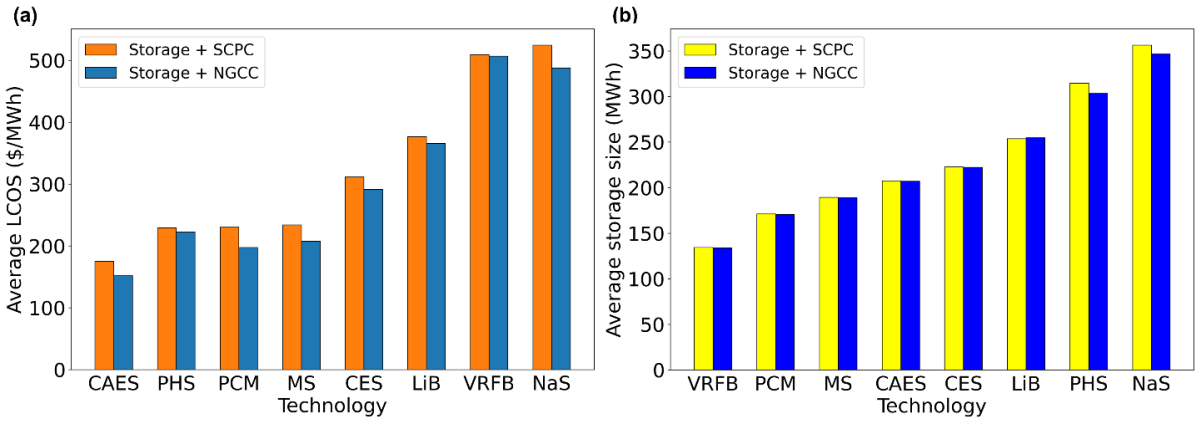

We also found that the average storage size, shown by Exhibit 4-5b, is nearly the same for the integration with both SCPC and NGCC power plants. The average storage size for long duration storage technologies, i.e., PHS and NaS batteries, was found to be higher for the integration with SCPC power plants as compared to the integration with NGCC power plants. A representative demand profile which has a higher integration size of PHS with the SCPC power plant than with the NGCC power plant is shown in Figure 4-6. For integration with SCPC plants (Figure 4-6b), the power plant operates at reduced load as compared to the integration with NGCC plants (Figure 4-6a). Due to the high operating costs associated with SCPC power plants, there is more emphasis on operating the power plant at lower load. Thus, the amount of demand met using power discharged by the energy storage increases for SCPC plants, which requires a larger storage system.

Exhibit 4-6: Operational profiles of PHS integration with (a) NGCC power plant and (b) SCPC power plant

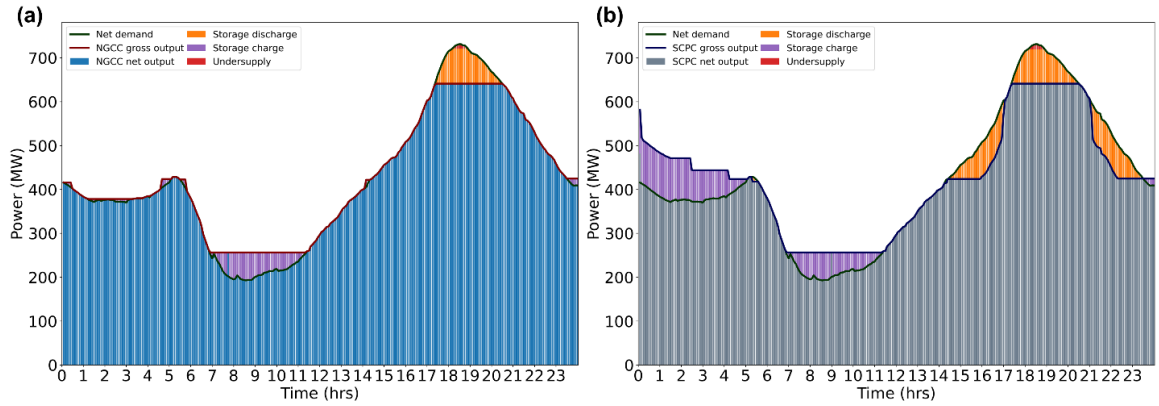

Considering optimal storage technologies for both NGCC and SCPC plants, as well as the results obtained by evaluating various scenarios, the following **6 technologies were downselected for detailed simulation and enhanced TEA: CAES, MS, PHS, CES, H_2 storage, and LiB.** It should be noted that while MS and PCM exhibit similar economics, only MS is selected to avoid repeating

study on similar technologies and as MS is more matured than PCM. Detailed TEA for these technologies is presented in subsequent sections.

5 CRYOGENIC ENERGY STORAGE

PROCESS DESCRIPTION

A diagram of the cryogenic energy storage process is shown in Exhibit 5-5.

Exhibit 5-4. Block Flow Diagram of the Cryogenic Energy Storage Process

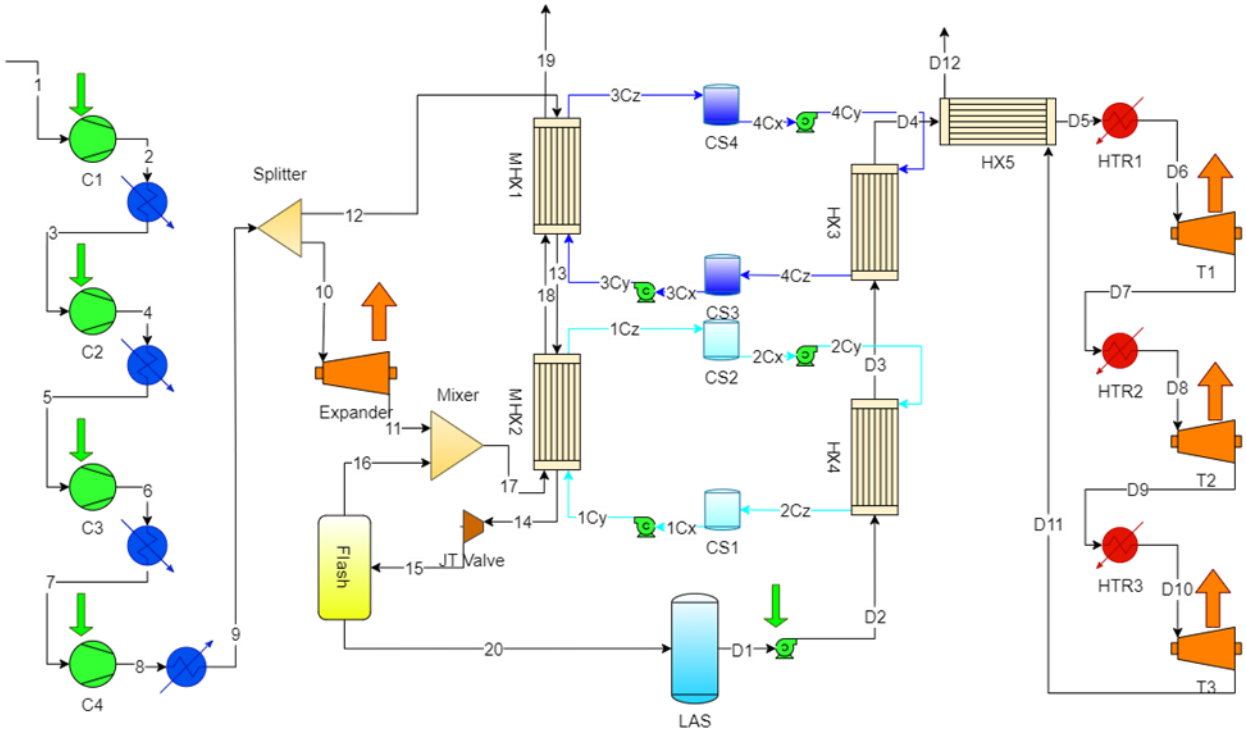

STREAM TABLES

Following section provides streams tables of the cryogenic energy storage process under the nominal design condition.

Exhibit 5-2. Stream Tables of the Cryogenic Energy Storage Process

Charging streams:

Stream	x_{N_2}	$\dot{m}$ (kg/s)	P (bar)	T ($°C$)	h (kJ/kg)	s (kJ/kg K)
1	0.77	337.68	1.00	20.00	-5.28	0.14
2	0.77	337.68	3.32	159.79	136.44	0.19
3	0.77	337.68	3.32	25.00	-0.76	-0.19
4	0.77	337.68	11.01	167.28	143.49	-0.14
5	0.77	337.68	11.01	25.00	-2.52	-0.54
6	0.77	337.68	36.55	167.91	142.18	-0.49
7	0.77	337.68	36.55	25.00	-8.19	-0.90
8	0.77	337.68	121.29	169.31	138.48	-0.85
9	0.77	337.68	121.29	25.00	-24.56	-1.30
10	0.77	45.59	121.29	25.00	-24.56	-1.30
11	0.77	45.59	1.01	-170.04	-197.96	-0.92
12	0.77	292.09	121.29	25.00	-24.56	-1.30
13	0.77	292.09	121.29	-53.00	-127.23	-1.70
14	0.77	292.09	121.29	-179.04	-389.82	-3.48
15	0.92	292.09	1.00	-193.96	-389.82	-3.27
16	0.92	53.29	1.00	-193.96	-227.65	-1.30
17	0.85	98.88	1.00	-183.17	-213.95	-1.11
18	0.85	98.88	1.00	-55.19	-82.08	-0.19
19	0.85	98.88	1.00	7.95	-17.63	0.07
20	0.74	238.80	1.00	-193.96	-426.01	-3.72

Internal coolant cycle streams:

Stream	Fluid	$\dot{m}$ (kg/s)	P (bar)	T ($°C$)	h (kJ/kg)	s (kJ/kg K)
1CY	Propane	258.46	1	-183	-3194.72	-10.25
1CZ	Propane	258.46	1	-61	-2948.38	-8.54
2CY	Propane	258.46	1	-59	-2944.03	-8.52
2CZ	Propane	258.46	1	-185	-3198.56	-10.30
3CY	Methanol	138.31	1	-55	-7648.56	-8.30
3CZ	Methanol	138.31	1	18	-7477.77	-7.62
4CY	Methanol	138.31	1	20	-7472.78	-7.61
4CZ	Methanol	138.31	1	-57	-7653.02	-8.32

Discharging side streams:

Stream	x_{N_2}	$\dot{m}$ (kg/s)	P (bar)	T ($°C$)	h (kJ/kg)	s (kJ/kg K)
D1	0.74	238.80	1.00	-193.96	-426.01	-3.72
D2	0.74	238.80	111.61	-189.18	-409.45	-3.66
D3	0.74	238.80	111.61	-59.74	-134.06	-1.69
D4	0.74	238.80	111.61	19.43	-29.70	-1.27
D5	0.74	238.80	111.61	19.43	-29.70	-1.27
D6	0.74	238.80	111.61	162.00	130.31	-0.83
D7	0.74	238.80	23.18	18.09	-12.49	-0.77
D8	0.74	238.80	23.18	162.00	136.48	-0.35
D9	0.74	238.80	4.81	20.48	-5.68	-0.30
D10	0.74	238.80	4.81	162.00	138.04	0.10
D11	0.74	238.80	1.01	21.84	-3.42	0.15

PERFORMANCE SUMMARY

Following section provides performance summary of the cryogenic energy storage process under the nominal design condition.

Exhibit 5-3. Performance Summary of the Cryogenic Energy Storage Process

Compressor 1 Work (MWe)	**47.86**
Compressor 2 Work (MWe)	48.71
Compressor 3 Work (MWe)	48.86
Compressor 4 Work (MWe)	49.53
Expander Work (MWe)	-7.9
Turbine 1 Work (MWe)	-34.1
Turbine 2 Work (MWe)	-33.94
Turbine 3 Work (MWe)	-33.78
Pump Work (MWe)	3.95
Round Trip Efficiency	0.52

MAJOR EQUIPMENT

Following section provides major equipment items of the cryogenic energy storage process.

Exhibit 5-4. Major Equipment Items of the Cryogenic Energy Storage Process

Equipment No.	Description	Type	Design condition	Qty.
1	Compressor	Air/Gas compressor	50MW power, output pressure max at 130 bar	4
2	Turbine	Air Turbine	Input pressure from 130 bar, temperature range from 20 – 170 $°C$	3
3	Heat Exchangers	Multi-stream heat exchangers, liquid-liquid heat exchange	shell-and-tube, operable at cryogenic temperatures (-195$°C$)	4
4	Expander	Gas expander/turbine	Operable over cryogenic temperatures	1
5	Heat Exchangers	Gas-liquid heat exchange	shell-and-tube, compatible with Dowtherm-G	7
6	Storage tanks	Commercial storage tanks	Operable at cryogenic temperatures	4
7	Flash	Phase separator	Cryogenic temperature operation	1

CAPITAL COST

Following section provides capital cost of the major equipment items of the cryogenic energy storage process.

Exhibit 5-5. Capital Cost of the Cryogenic Energy Storage Process

Item	Cost	Labor and Material		Bare erected cost	Contingency	Capital Cost 2021	
	($)	Direct Costs ($)	Indirect costs ($)	($)	($)	$/kW	$/kWh
Compressor 1	5143321	3446025	1202508	9791855	489593	102.81	
Compressor 2	5200061	3484041	1215774	9899876	494994	103.95	
Compressor 3	5209910	3490640	1218077	9918626	495931	104.15	
Compressor 4	5253803	3520048	1228339	10002191	500110	105.02	
Expander	1131124	757853	264457	2153433	107672	22.61	
Turbine 1	6480122	4341682	1515052	12336856	616843	129.54	
Turbine 2	6456647	4325953	1509564	12292164	614608	129.07	
Turbine 3	6430510	4308441	1503453	12242404	612120	128.55	
Pump	2067388	1385150	483355	3935894	196795	41.33	
CLR 1	1596000	1069320	373145	3038464	151923	31.90	
CLR 2	1664950	1115516	389265	3169732	158487	33.28	
CLR 3	1698551	1138029	397121	3233702	161685	33.95	
CLR 4	1962100	1314607	458739	3735446	186772	39.22	
HTR 1	2455727	1645337	574149	4675214	233761	49.09	
HTR 2	2335580	1564839	546059	4446478	222324	46.69	
HTR 3	2279359	1527170	532914	4339443	216972	45.56	
MHE 1	3047643	2041921	712539	5802102	290105	60.92	
MHE 2	1381828	925825	323071	2630723	131536	27.62	
MHE 3	2765461	1852859	646565	5264885	263244	55.28	
MHE 4	6386519	4278968	1493168	12158655	607933	127.67	
Flash	1773	1188	415	3375	169	0.04	
Tank 1 - Methanol	2011744	1347869	470346	3829959	191498		10.05
Tank 2 - Propane	10814831	7245937	2528507	20589275	1029464		54.05
Tank 3 - Air	1264823	847432	295716	2407971	120399		6.32
Tank 4 - Thermal oil	1600000	1072000	374080	3046080	152304		8.00
Dowtherm-G	34528029	23133779	8072653	65734461	3286723		172.55
Methanol	1989472	1332946	465138	3787556	189378		9.94
Propane	1033720	692592	241684	1967996	98400		5.17
Total	**124190996**	**83207967**	**29035855**	**236434817**	**11821741**	**1418.25**	**266.08**

*Additional Owners cost computed at 10% of bare erected costs and additional material replacement cost annual computed for Dowtherm-G, methanol, and propane to be at $1,877,561/year.

OPERATING & MAINTENANCE COST

Following section provides operating and maintenance costs under base, moderate and extreme operating conditions of the cryogenic energy storage process.

Exhibit 5-6. Operating & Maintenance Cost of the Cryogenic Energy Storage Process

	Base	Moderate	Extreme
Charging Power (MW)	93.00	46.16	72.75
Discharging Power (MW)	98.00	101.82	63.42
Storage Size (MWh)	400.00	209.24	166.35
Fixed O&M costs			
Operating Labor costs	$1,355,503.10	$861,739.52	$829,188.64
Maintenance Labor costs	$1,355,503.10	$861,739.52	$829,188.64
Property taxes	$5,422,012.41	$3,446,958.08	$3,316,754.56
Insurance	$2,711,006.20	$1,723,479.04	$1,658,377.28
Variable O&M Costs	$5,422,012.41	$3,446,958.08	$3,316,754.56
Replacement Dowtherm-G	$1,726,401.44	$1,097,532.24	$1,056,074.65
Replacement Propane	$99,473.58	$63,238.75	$60,850.00
Replacement Methanol	$51,686.00	$32,858.55	$31,617.37
Total O&M costs	$18,143,598.25	$11,534,503.78	$11,098,805.69
Charging costs	$8,368,360.72	$4,370,950.92	$3,476,485.94

LCOS

Following section provides LCOS of the cryogenic energy storage process.

Exhibit 5-7. LCOS of the Cryogenic Energy Storage Process

Component	Value $/MWh	Percentage
Capital	196.97	74%
Fixed O&M	7.88	3%
Variable O&M	5.30	2%
Electricity	57.32	21%
Total	267.47	100%

6 High Temperature Thermal Energy Storage (HTTS) Using Molten Salt

Process Description

A diagram of the high temperature thermal energy storage is shown in Exhibit 6-6.

Exhibit 6-5. Block Flow Diagram of the HTTS

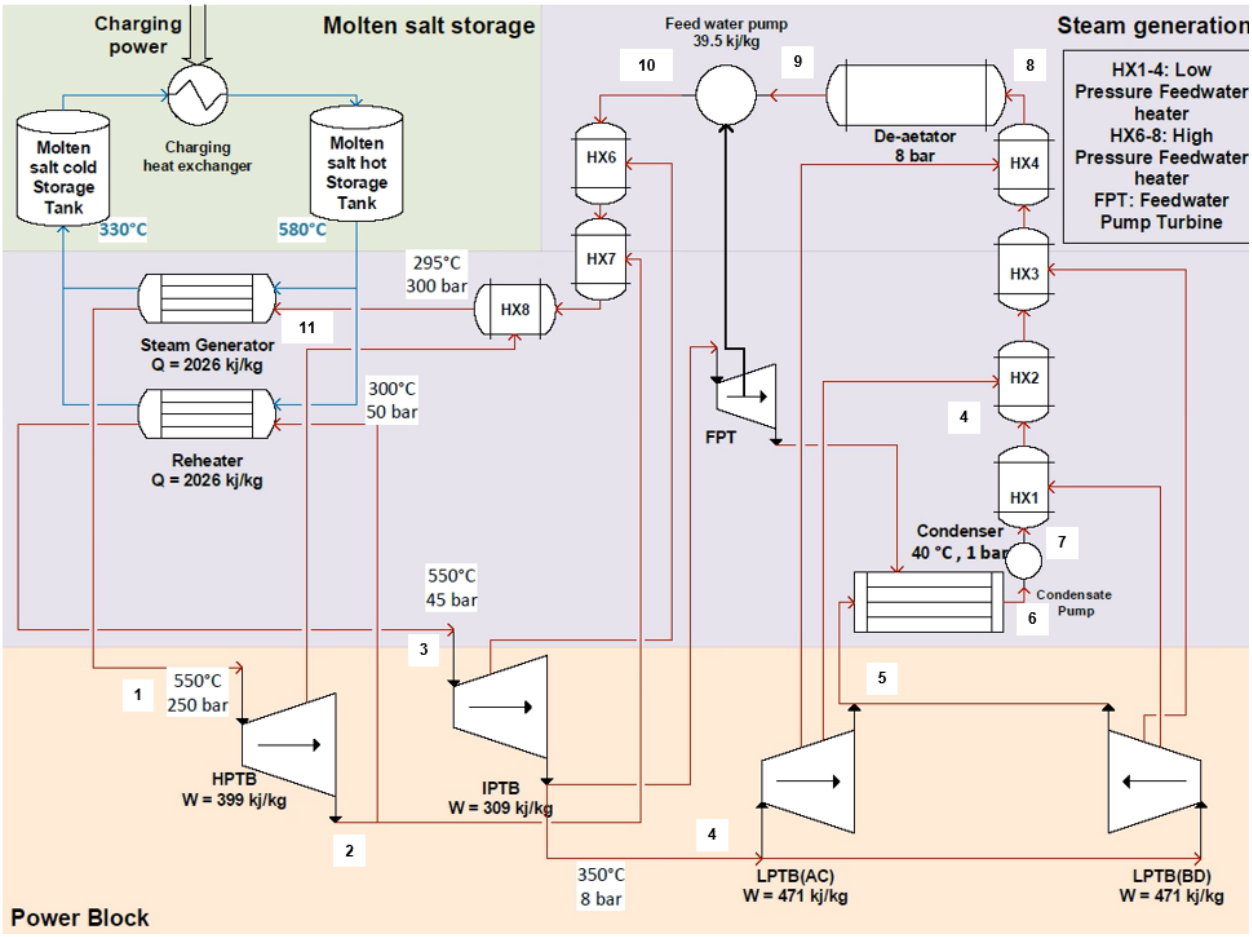

STREAM TABLES

Following section provides streams tables of the HTTS process under the nominal design condition corresponding to the process flow diagram shown in Exhibit 6-1.

Exhibit 6-2. Stream Tables of the HTTS Process

Water/Steam Stream Tables:

State	Position	Flow rate (kg/s)	Pressure (MPa)	Temperature (°C)	Enthalpy (kJ/kg)	Vapor fraction
1	HP turbine inlet	84.82	25	550	3300	1
2	HP turbine outlet	77.78	4.5	550	2926	1
3	Reheat turbine inlet	69.38	4.5	350	3556	1
4	LP turbine inlet	64.26	0.8	350	3162	1
5	LP turbine outlet (quality region)	55.51	0.01	47	2417	0.93
6	Hot well outlet (subcooled liquid)	84.82	0.01	40	168	0
7	Condensate Pump outlet	84.82	0.8	170	168	0
9	Open Feedwater Heater (saturated liquid)	84.82	0.8	170	721	0
10	Feedwater Pump outlet (compressed liquid)	84.82	30	175	756	0

Molten Salt Streams Table:

	Position	Flow rate (kg/s)	Pressure (MPa)	Temperature (°C)
MS1	Steam generator outlet	8.61	0.1013	330
MS2	Steam generator inlet	8.61	0.1013	580
MS3	Reheater outlet	3.86	0.1013	330
MS4	Reheater inlet	3.86	0.1013	580

PERFORMANCE SUMMARY

Following section provides performance summary of the HTTS process under the nominal design condition.

Exhibit 6-3. Performance Summary of the HTTS Process

Unit	Value
High Pressure Steam Turbine (HPTB) Work	33.84 MWe
Intermediate Pressure Steam Turbine (IPTB) Work	26.20 MWe
Low Pressure Steam Turbine (HPTB) Work	39.95 MWe
Steam Generator Heat Transfer Rate	168.79 MWe
Reheater Heat Transfer Rate	75.66 MWe
Round Trip Efficiency	0.3862

MAJOR EQUIPMENT

Following section provides major equipment items of the HTTS process.

Exhibit 6-4. Major Equipment Items of the HTTS Process

Equipment No.	Description	Type	Design condition	Qty.
1	Pump	Water pump	Feed water pump (39 kWe) and condensate pump	2
2	Turbine	Steam turbine	1 HPTB, 1 IPTB and 2 LPTB with 80% isentropic efficiency and 80% mechanical efficiency	4
3	Heat Exchangers	Preheater	Steam generator feed water heater, Hot streams are steam extracted from turbine	8
4	Heat Exchanger	Boiler	Steam generator, steam heated by molten salt	1
5	Heat Exchanger	Reheater	Shell-and-tube	1
6	Storage tanks	Commercial storage tanks	Molten salt hot and cold storage tank	2
7	Condenser	Cooling tower	40 °C 1 atm	1
8	Molten salt pump	Liquid pump	Temperature limit is higher than 600 °C	1

CAPITAL COST

Following section provides capital cost of the major equipment items of the HTTS process.

Exhibit 6-5. Capital Cost of the HTTS Process

Item	Cost	Labor and Material		Bare erected cost	Contingency	Capital Cost 2021	
	($)	Direct Costs ($)	Indirect costs ($)	($)	($)	$/kW	$/kWh
Molten Salt	4,153,539.6	2,782,871.5	971,097.6	7,907,508.7	395,375.4		20.8
Hot Storage Tank	1,447,656.5	969,929.9	338,462.1	2,756,048.5	137,802.4		7.2
Cold Storage Tank	3,813,146.8	2,554,808.4	891,513.7	7,259,469.0	362,973.4	76.2	
HPTB	4,406,224.3	2,952,170.3	1,030,175.2	8,388,569.9	419,428.5	88.1	
IPTB	2,987,252.0	2,001,458.8	698,419.5	5,687,130.3	284,356.5	59.7	
LPTB	3,666,323.7	2,456,436.9	857,186.5	6,979,947.1	348,997.4	73.3	
Steam generator	5,603,005.0	3,754,013.4	1,309,982.6	10,667,000.9	533,350.0	112.0	
pumps	1,281,800.0	858,806.0	299,684.8	2,440,290.8	122,014.5	25.6	
Preheaters	461,712.0	309,347.0	107,948.3	879,007.3	43,950.4	9.2	
Reheaters	3,169,523.0	2,123,580.4	741,034.5	6,034,137.9	301,706.9	63.4	
Total	30,990,183.0	20,763,422.6	7,245,504.8	58,999,110.3	2,949,955.5	507.5	28.0

OPERATING & MAINTENANCE COST

Following section provides operating and maintenance costs under base, moderate and extreme operating conditions of the HTTS process.

Exhibit 6-6. Operating & Maintenance Cost of the HTTS Process

	Base	Moderate	Extreme
Charging Power (MW)	100	3975	3975
Discharging Power (MW)	100	101.82	63.44
Storage Size (MWh)	400	209.24	128.69
Fixed O&M costs			
Operating Labor costs	$206,628	$179,474	$163,745
Maintenance Labor costs	$206,628	$179,474	$163,745
Property taxes	$826,513	$717,897	$654,980
Insurance	$413,256	$358,948	$327,490
Variable O&M Costs	$470,000	$478,554	$298,168
Total O&M costs	$2,123,027	$1,914,348	$1,608,1283
Charging costs	$11,367,276	$5,937,340	$4,722,331

LCOS

Following section provides LCOS of the HTTS process.

Exhibit 6-7. LCOS of the HTTS Process

Component	Value $/MWh	Percentage
Capital	66.49	42%
Fixed O&M	11.32	7%
Variable O&M	3.22	2%
Electricity	77.68	49%
Total	158.72	100%

7 COMPRESSED AIR ENERGY STORAGE

PROCESS DESCRIPTION

A diagram of the compressed air energy storage (CAES) is shown in Exhibit 7-1.

Exhibit 7-1. Block Flow Diagram of the CAES Process

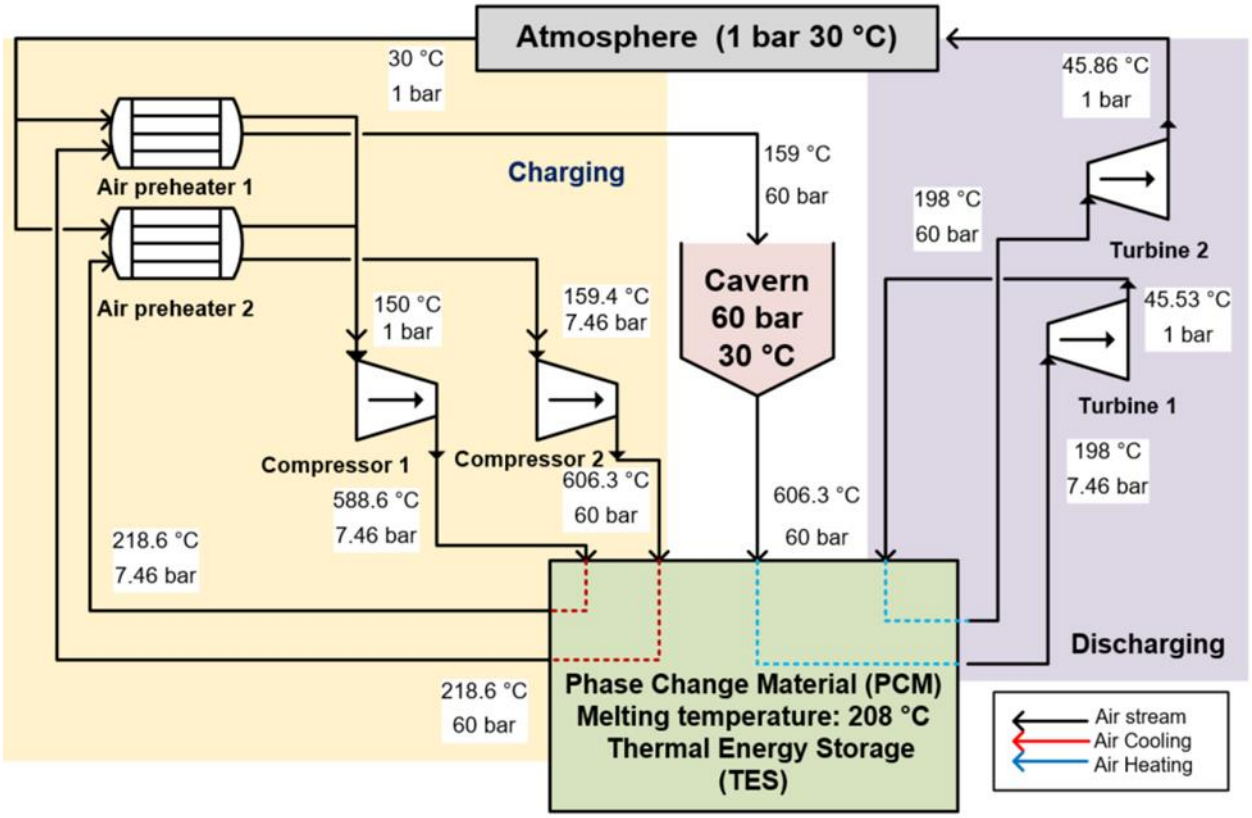

STREAM TABLES

Following section provides streams tables of the CAES process under the nominal design condition corresponding to the process flow diagram shown in Exhibit 7-1.

Exhibit 7-2. Stream Tables of the CAES Process

Column1	Temperature (°C)	Pressure (bar)
Air preheater 1 hot stream inlet	218.6	60
Air preheater 1 hot stream outlet	159	60
Air preheater 1 cold stream inlet	30	1
Air preheater 1 cold stream outlet	149	1
Air preheater 2 hot stream inlet	218.6	7.46
Air preheater 2 hot stream outlet	159.4	7.46
Air preheater 2 cold stream inlet	30	1
Air preheater 2 cold stream outlet	150	1
Compressor 1 outlet	588.6	7.46
Compressor 2 outlet	606.3	60
Expander/Turbine 1 inlet	198	60
Expander/Turbine 2 inlet	198	7.46
Expander/Turbine 1 outlet	45.53	7.46
Expander/Turbine 2 outlet	45.53	1

PERFORMANCE SUMMARY

Exhibit 7-3. Performance Summary of the CAES Process

Equipment	Work
Compressor 1 (MWe)	**371.9**
Compressor 2 (MWe)	381.4
Expander 1 (MWe)	129.3
Expander 1 (MWe)	129.1
Round Trip Efficiency	34.3%

Note: For CAES round trip efficiency varies with carven pressure, this work and efficiency is based on 30 bar carven pressure

MAJOR EQUIPMENT

Exhibit 7-4. Major Equipment Items of the CAES Process

Equipment No.	Description	Type	Design condition	Qty.
1	Compressor	Air compressor	380 MW power, output pressure max at y bar	2
2	Heat Exchangers	Air preheater	shell-and-tube,	2
3	Expander	Gas expander/turbine	150 MW power	2

CAPITAL COST

Exhibit 7-5. Capital Cost of the CAES Process

Item	Cost	Labor and Material		Bare erected cost	Contingency	Capital Cost 2021	
	($)	Direct Costs ($)	Indirect costs ($)	($)	($)	$/kW	$/kWh
Compressor	$17,144,321	$11,486,695	$4,008,342	$32,639,359	$171,443	$171	
Expander	$265,111	$177,624	$61,983	$504,718	$2,651	$3	
Air preheater	$32,541,200	$21,802,604	$7,608,133	$61,951,937	$325,412		$814
PCM storage	$17,144,321	$11,486,695	$4,008,342	$32,639,359	$171,443	$171	
Total	$7,768,814	$5,205,105	$1,816,349	$14,790,267	$77,688	$78	

OPERATING & MAINTENANCE COST

Exhibit 7-6. Operating & Maintenance Cost of the Compressed Air Energy Storage Process

	Base	Moderate	Extreme
Charging Power (MW)	100	25.14	32.91
Discharging Power (MW)	100	51.33	50.43
Storage Size (MWh)	400	104.83	75.31
Fixed O&M costs	$ 228,810.00	$ 72,570.32	$ 64,030.78
Operating Labor costs	$ 228,810.00	$ 72,570.32	$ 64,030.78
Maintenance Labor costs	$ 915,240.00	$ 290,281.27	$ 256,123.14
Property taxes	$ 457,620.00	$ 145,140.63	$ 128,061.57
Insurance	$ 1,830,480.00	$ 580,562.53	$ 512,246.27
Total O&M costs	$ 457,620.00	$ 145,140.63	$ 128,061.57
Charging costs	$ 1,830,480.00	$ 580,562.53	$ 512,246.27

LCOS

Exhibit 7-7. LCOS of the Compressed Air Energy Storage

Component	Value $/MWh	Percentage
Capital	68.2	45%
Fixed O&M	42.8	8.5%
Variable O&M	0	0%
Electricity	70.4	46.5%
Total	151.4	100%

8 HYDROGEN STORAGE

PROCESS DESCRIPTION

A diagram of the hydrogen storage is shown in Exhibit 8-7. H_2 is generated using the PEM electrolyzer and then compressed and cooled for sending to the storage. Gas is expanded through an expander before sending it to the NGCC GT combustor as shown in Exhibit 8-1.

Exhibit 8-6. Block Flow Diagram of the Hydrogen Injection to NGCC

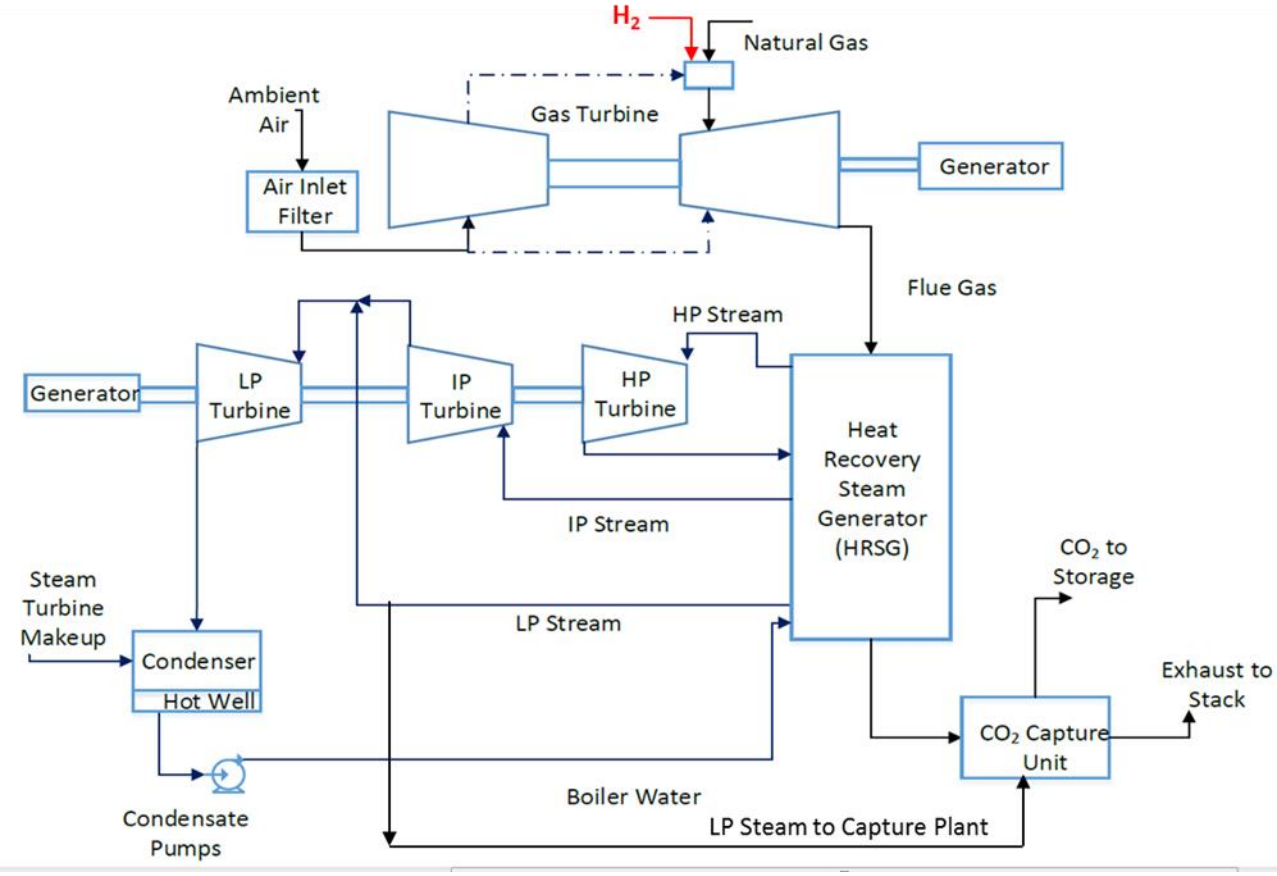

NOMINAL OPERATING CONDITIONS

Compression system from 30 bar to 100 bar at 40°C
Nominal H_2 flow rate = 4213 kg/hr.
Inlet charging power (compressor) = 1 kWh/kg

PERFORMANCE SUMMARY

Round trip efficiency=0.27

MAJOR EQUIPMENT

Exhibit 8-2. Major Equipment Items of the Hydrogen Storage Process

Equipment No.	Description	Type	Design condition	Qty.
1	Compressor	Gas compressor	607 kW power, output pressure max at 100 bar	1
2	Heat Exchangers	Gas-cooling water heat exchange	shell-and-tube,	1
3	Electrolyzer	PEM	5.6kW capacity each	7008
4	Turbine	Gas turbine	100 bar to 30 bar	1

CAPITAL COST

Exhibit 8-3. Capital Cost of the Hydrogen Storage Process

Item	Cost	Labor and Material		Bare erected cost	Contingency	Capital Cost 2021	
	($)	Direct Costs ($)	Indirect costs ($)	($)	($)	$/MW	$/MWh
Charging cycle (Compressor + Electrolyzer)	13005200	-	-	-	-	325130	
Storage	600480						22240
Discharging cycle	2457805					37607	
Total	**16,063,485**						

*Additional Owners cost computed at 10% of bare erected costs (Direct indirect costs can be computed based on local installation cost)

* Electrolyzer replacement cost not included

OPERATING & MAINTENANCE COST

Exhibit 8-4. Operating & Maintenance Cost of the Hydrogen Storage Process

	Moderate	Extreme
Charging Power (MW)	39.24	69.58
Discharging Power (MW)	65.35	144.78
Storage Size (MWh)	27.23	84.46
Fixed O&M costs	$82,125	$149,949
Variable O&M Costs	$34,788	$107,894
Charging Costs	$1,104,380	$1,712,662

LCOS

LCOS breakdown provided for the moderate case.

Exhibit 8-5. LCOS of the Hydrogen Storage

Component	Value $/MWh	Percentage
Capital	412.56	77.05%
Fixed O&M	8.26	1.54%
Variable O&M	3.50	0.66%
Electricity	111.11	20.75%
Total	535.43	100%

9 LI-ION BATTERY STORAGE

PROCESS DESCRIPTION

Exhibit 9-8 shows the typical Li-Ion battery. It should be noted that the Li-Ion battery is neither integrated with NGCC or SCPC plant, but that since this project is evaluating decentralized storage at the site of power plant, the max power consumption for charging the battery cannot exceed the power production by the host plant at the host plant. Similarly, during discharge, the total power produced by the host plant and the battery should not exceed the max rated power of the host power plant.

Exhibit 9-7. Schematic of the Li-Ion Battery

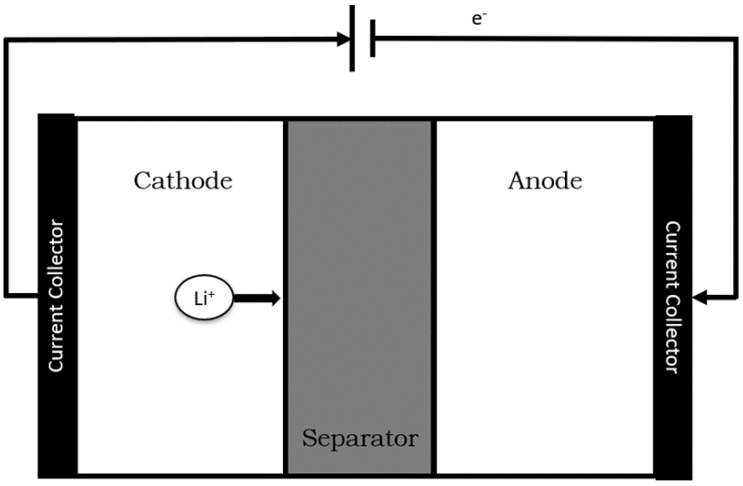

KEY DESIGN VARIABLES

Nominal Energy capacity: 397 MWh

Nominal Power capacity: 99.31 MW

PERFORMANCE SUMMARY

Round-trip efficiency = 95%

CAPITAL COST

Capital cost = $203,933,520

OPERATING & MAINTENANCE COST

Costs are reported on annual basis.

Fixed O&M = $376,315
Variable O&M = $44,715

LCOS

Exhibit 9-2. LCOS of the Li-Ion Battery Storage

Component	Value $/MWh	Percentage
Capital	289.12	88.59%
Fixed O&M	5.02	1.54%
Variable O&M	0.60	0.18%
Electricity	31.57	9.67%
Total	326.33	100%

10 PUMPED HYDRO STORAGE

PROCESS DESCRIPTION

A diagram of the pumped hydro storage is shown in Exhibit 10-9**Error! Reference source not found.**.

Exhibit 10-8. Block Flow Diagram of the Pumped Hydro Storage Process

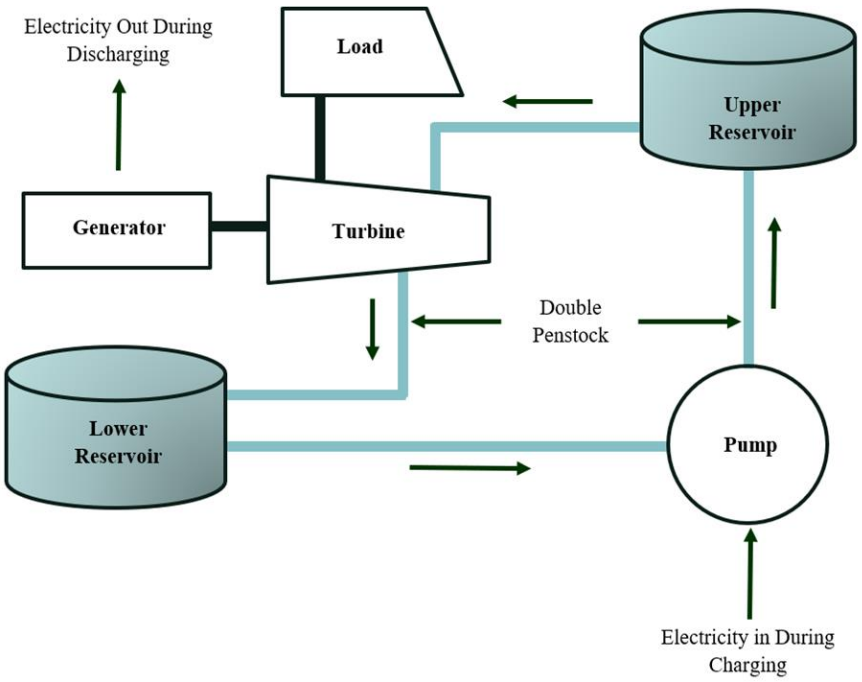

KEY DESIGN VARIABLES

Note that the values are provided for the moderate case.

Storage capacity = 205.96 MWh

Power capacity (charging) = 400 MW

Power capacity (discharging) = 94.56 MW

PERFORMANCE SUMMARY

Round-trip efficiency = 0.81

CAPITAL COST

Capital cost = $200,422,411

OPERATING & MAINTENANCE COST

Fixed O&M Cost = $1,891,678
Variable O&M Cost = $188

LCOS

Exhibit 10-2. LCOS of the Pumped Hydro Storage

Component	Value $/MWh	Percentage
Capital	282.12	81.95%
Fixed O&M	25.10	7.29%
Variable O&M	0.002	0.00%
Electricity	37.03	10.76%
Total	344.27	100%

11 CONCLUDING REMARKS

In this project, optimal storage technologies integrated with NGCC and SCPC plants were obtained through downselection of promising energy storage technologies. Detailed models of most of the energy storage technologies were developed. First-principles models of NGCC and SCPC plants were used for developing ROM that were then used for optimization. By minimizing LCOS under a number of scenarios for both NGCC and SCPC plants, it was observed that the top storage technologies are - CES, HTTS, MS, PHS, H_2 storage, and Li-Ion battery. For HTTS, molten salt is considered, even though PCM was also found to be very competitive.

It was observed that the ranking of the optimal storage technology can differ based on the host power plant technology even when same demand/supply/price profile for electricity are considered. It was also observed that as the variability in power demand changes, the ranking of the optimal storage technologies also changes. However, for the same demand and LMP profile, the top six optimal storage technologies for NGCC vs SCPC plants did not differ much even though LCOS for the same technology and optimal size of a given storage technology did differ.

This project did not include any constraints on the size/location for CAES and PHS, and also assumed decoupled operation of NGCC GT and feasibility of operation of existing F-class frame with 20 wt% H_2.

The model-based approach and optimization framework developed in this project for optimal selection and operation of energy storage technologies is generic and can screen/optimize more storage technologies as needed. The approach and framework can be readily applied to centralized (i.e., stand-alone) storage technologies as well.

In the future, the team looks forward to enhancing the capabilities of the software, considering additional energy storage technologies, and experimental validation of the predicted transient performance of the storage technologies.

PRODUCTIVITIES

Publications

1. Zantye, M. S., Gandhi, A., Wang, Y., Vudata, S. P., Bhattacharyya, D., & Hasan, M. F. (2022). Optimal design and integration of decentralized electrochemical energy storage with renewables and fossil plants. *Energy & Environmental Science,* 15, 4119-4136.
2. Gandhi, A., Zantye, M. S., & Hasan, M. F. (2022). Cryogenic energy storage: Standalone design, rigorous optimization and techno-economic analysis. *Applied Energy*, 322, 119413.
3. Gandhi, A., Zantye, M. S., & Hasan, M. F. (2022). Integration of cryogenic energy storage with renewables and power plants: Optimal strategies and cost analysis. *Energy Conversion and Management*, 269, 116165.
4. Zantye, M. S., Gandhi, A., Li, M., Arora, A., & Hasan, M. F. (2022). A Systematic Framework for the Integration of Carbon Capture, Renewables and Energy Storage Systems for Sustainable Energy. In *Computer Aided Chemical Engineering* (Vol. 49, pp. 2089-2094). Elsevier.
5. Arora, A., Zantye, M. S., & Hasan, M. F. (2022). Sustainable hydrogen manufacturing via renewable-integrated intensified process for refueling stations. *Applied Energy*, 311, 118667.
6. Zantye, M. S., Gandhi, A., Wang, Y., Vudata, S. P., Bhattacharyya, D., & Hasan, M. F. (2023). THESEUS: A Techno-Economic Design, Integration and Downselection Framework for Energy Storage. *Energy Conversion and Management*, 284, 116976.
7. Sengalini P, Haque M E, Zantye, M. S., Gandhi, A., Li M, Bhattacharyya, D., & Hasan, M. F. (2023). Techno-Economic Analysis and Optimization of a Compressed Air Energy Storage System Integrated with a Natural Gas Combined Cycle Plant. *Energies,* 16, 4867

Presentations

1. Manali S. Zantye, Akhilesh Gandhi, Mengdi Li, Pavitra Senthamilselvan Sengalani, Yifan Wang, Sai Pushpitha Vudata, Debangsu Bhattacharyya and Faruque Hasan. THESEUS: An Optimal Design and Downselection Framework for Energy Storage Technologies. Presented at the AIChE Annual Meeting, Phoenix, AZ, November 14, 2022.
2. Akhilesh Gandhi, Manali S. Zantye and Faruque Hasan. Cryogenic Energy Storage: Design, Techno-Economic Analysis, and Integration with Power Plants and Renewables. Presented at the AIChE Annual Meeting, Phoenix, AZ, November 17, 2022.
3. Manali S. Zantye, Akhilesh Gandhi, Akhil Arora, and M. M. Faruque Hasan. A Systematic Framework for the Integration of Carbon Capture, Renewables and Energy Storage Systems for Sustainable Energy. In Process Systems Engineering (*PSE21+)* Conference, Virtual poster, 2022.

4. Manali S. Zantye, Akhilesh Gandhi, Mengdi Li, Yifan Wang, Sai Pushpitha Vudata, Pavitra Senthamilselvan Sengalani, Debangsu Bhattacharyya, M.M. Faruque Hasan. An Optimization-Based Decision Framework for Integrating Energy Storage with Fossil Power Plants. Presented at the AIChE Annual Meeting, Boston, MA, November 10, 2021.
5. Mengdi Li, Akhilesh Gandhi, Manali S. Zantye and M. M. Faruque Hasan. Design and Integration of Thermal Energy Storage Systems for Power Plants. Presented at the AIChE Annual Meeting, Boston, MA, November 10, 2021.
6. Manali S. Zantye, Mengdi Li, Yifan Wang, Sai Pushpitha Vudata, Pavitra Senthamilselvan Sengalani, Debangsu Bhattacharyya, M. M. Faruque Hasan. A Decision Framework for Integrating Energy Storage with Power Plants: Technology Selection, Design and Optimization. Presented at the AIChE Annual Meeting, Virtual, November 17, 2020.
7. Mengdi Li, Manali S. Zantye, Debangsu Bhattacharyya, M.M. Faruque Hasan. Modeling and Optimization of High-Temperature Thermal Storage (HTTS) Integrated with Fossil-Fueled Power Plants. Presented at the AIChE Annual Meeting, Virtual, November 17, 2020.

REFERENCES

Bhattacharyya D, Rengaswamy R, "System Identification and Nonlinear Model Predictive Control of Solid-Oxide Fuel Cell", Ind. Eng. Chem. Res. 49, 4800 – 4808, 2010

Blaabjerg F, Consoli A, Ferreira J A, VanWyk J D, "The Future of Electronic Power Processing and Conversion," IEEE Trans. Power Electron., 20, 715–720, 2005
Connolly D, MacLaughlin S, Leahy M, "Development of a computer program to locate potential sites for pumped hydroelectric energy storage," Energy, 35, 375–381, 2010

Colbertaldo P., Aláez S, and Campanari S., "Zero-dimensional dynamic modeling of PEM electrolyzers Assessing feasibility of using the heat temperature function for a long-term district heat demand forecast," *Energy Procedia*, vol. 142, pp. 1468–1473, 2017

Crotogino F, Mohmeyer K U, and Scharf R, "Huntorf CAES: More than 20 Years of Successful Operation," *Solut. Min. Res. Inst. Spring Meet.*, April, pp. 351–357, 2001
Görgün H, "Dynamic modelling of a proton exchange membrane (PEM) electrolyzer," 31, 29–38, International Journal of Hydrogen Energy, 2006

Deane J P, Gallachóir B P Ó, McKeogh E J, "Techno-economic review of existing and new pumped hydro energy storage plant," Renew. Sustain. Energy Rev., 14, 1293–1302, 2010

Gu F C, Chen H C, Li K Y, "Mathematic Modeling and Performance Analysis of Vanadium Redox Flow Battery," Energy & Fuels, 34, 10142–10147, 2020.

Kawamoto H, Kusakabe Y, "Performance and Thermal Behavior of Sodium-Sulfur Cell under High Current Density Operations", Journal of the Electrochemical Society, 136 , 1355-1361, 1989

Lourenssen K, Williams J, Ahmadpour F, Clemmer R, Tasnim S, "Vanadium redox flow batteries: A comprehensive review," J. Energy Storage, 25, 100844, 2019

Lawder, M T, "Modeling, Simulation, and Analysis of Lithium-Ion Batteries for Grid-Scale Applications" (2016). Engineering and Applied Science Theses & Dissertations. 164.

Northrop P W C , Ramadesigan V, De S, Subramanian V R, "Coordinate Transformation, Orthogonal Collocation, Model Reformulation and Simulation of Electrochemical-Thermal Behavior of Lithium-Ion Battery Stacks", J. Electrochem. Soc. 158, A1461, 2011

Persson M, Mignard D, and Hogg D, "Insights on performance and an improved model for full scale electrolyzer based on plant data for design and operation of hydrogen production," Int. J. Hydrogen Energy, vol. 45, no. 56, pp. 31396–31409, 2020.

Raju M, and Khaitan S K, "Modeling and simulation of compressed air storage in caverns: A case study of the Huntorf plant," *Appl. Energy*, 89, 474–481, 2012

Schaefer (Caprio) S, Vudata S P, Bhattacharyya D, Turton R, "Transient Modeling and Simulation of a Non-isothermal Sodium-sulfur Cell", Journal of Power Sources, 453, 227849, 2020

Sivakumar N, Das D, Padhy N P, Senthil Kumar A. R., and Bisoyi N, "Status of pumped hydro-storage schemes and its future in India," Renew. Sustain. Energy Rev., 19, 208–213, 2013.

Striednig M, Brandstätter S, Sartory M, Klell M, "Thermodynamic real gas analysis of a tank filling process," *Int. J. Hydrogen Energy*, 39, 8495–8509, 2014

U.S. Hydropower Market Report, co-authored by Uría-Martínez R, Johnson M M, Shan R, along with other co-authors, Water Power Technologies Office, EERE, U.S. DOE, 2021, available online at: https://www.energy.gov/sites/prod/files/2021/01/f82/us-hydropower-market-report-full-2021.pdf

Vudata S P, Bhattacharyya D, "Transient Modeling of a Vanadium Redox Flow Battery and Real-Time Monitoring of Its Capacity and State of Charge", 61, 17557-17571, Industrial & Engineering Chemistry Research, 2022

Wang Y, Bhattacharyya D, Turton, R, "Evaluation of Novel Configurations of Natural Gas Combined Cycle (NGCC) Power Plants for Load-Following Operation using Dynamic Modeling and Optimization", *Energy & Fuels*, 34,1053-1070, 2020

Xiao J, Bénard P, Chahine R, "Charge-discharge cycle thermodynamics for compression hydrogen storage system," *Int. J. Hydrogen Energy*, 41, 5531–5539, 2016

X. Yuan et al., "A review of all-vanadium redox flow battery durability: Degradation mechanisms and mitigation strategies," Int. J. Energy Res.,4607, 2019.